ESAIM: M2AN 56 (2022) 651–678
https://doi.org/10.1051/m2an/2022003

ESAIM: Mathematical Modelling and Numerical Analysis
www.esaim-m2an.org

FULLY-DISCRETE, DECOUPLED, SECOND-ORDER TIME-ACCURATE AND ENERGY STABLE FINITE ELEMENT NUMERICAL SCHEME OF THE CAHN-HILLIARD BINARY SURFACTANT MODEL CONFINED IN THE HELE-SHAW CELL

Xiaofeng Yang*

Abstract. We consider the numerical approximation of the binary fluid surfactant phase-field model confined in a Hele-Shaw cell, where the system includes two coupled Cahn-Hilliard equations and Darcy equations. We develop a fully-discrete finite element scheme with some desired characteristics, including linearity, second-order time accuracy, decoupling structure, and unconditional energy stability. The scheme is constructed by combining the projection method for the Darcy equation, the quadratization approach for the nonlinear energy potential, and a decoupling method of using a trivial ODE built upon the "zero-energy-contribution" feature. The advantage of this scheme is that not only can all variables be calculated in a decoupled manner, but each equation has only constant coefficients at each time step. We strictly prove that the scheme satisfies the unconditional energy stability and give a detailed implementation process. Various numerical examples are further carried out to prove the effectiveness of the scheme, in which the benchmark Saffman-Taylor fingering instability problems in various flow regimes are simulated to verify the weakening effects of surfactant on surface tension.

Mathematics Subject Classification. 65N12, 65M12, 65M70.

Received April 6, 2021. Accepted January 4, 2022.

1. Introduction

We consider the numerical approximation of the binary surfactant phase-field model confined in the Hele-Shaw cell in this paper, focusing on establishing a fully-discrete finite element scheme with desired properties of linearity, second-order temporal accuracy, decoupling structure, and unconditional energy stability (for simplicity, a numerical scheme with these properties is called as "ideal"). The term Hele-Shaw (or Hele-Shaw cell) is commonly used to describe the restricted movement of fluid between two parallel plates with a small gap. The fluid motion for this type of flow conforms to the mechanical principles in a porous medium. Surfactants, as a common compound that can change or reduce the interfacial tension of multiphase fluids, have been modeled and simulated for a long time using the phase-field method, see [18, 19, 25–27, 41, 42, 44, 45]. The main idea of using the phase-field approach to simulate a binary fluid mixture with surfactants is to adopt two phase-field variables, one for the local density of the fluid, and the other for the local concentration of surfactants. The total free energy incorporating the hydrophilic-hydrophobic interaction of the fluid and the interfacial absorption

---

Keywords and phrases. Finite element, fully-discrete, second-order, fluid-surfactant, Cahn-Hilliard, Hele-Shaw cell.

Department of Mathematics, University of South Carolina, Columbia, SC29208, USA.
*Corresponding author: `xfyang@math.sc.edu`

characteristics caused by the amphiphilic nature of surfactant molecules is postulated. By using the gradient flow method (Cahn-Hilliard dynamics) to minimize the free energy, a governing system composed of two highly nonlinear coupled Cahn-Hilliard equations can be obtained.

To simulate the free interface motion driven by the flow field (*e.g.*, droplets coalescence/non-merging phenomena under the shear flow, or Saffman-Taylor fingering instability in the porous medium flow, etc., see [12, 14, 16, 24, 28, 31, 34, 43, 56]), the hydrodynamic equations will be coupled with the two Cahn-Hilliard equations to obtain a full flow-coupled binary fluid surfactant model. Different fluid equations will be used in different flow regimes, such as the Navier-Stokes equations for incompressible fluids, the Darcy equations for the porous medium, etc. Obviously, due to the existence of more coupled nonlinear terms, designing numerical schemes for a flow-coupled model is far more difficult than that of a model without flow. Then, for the Darcy flow-coupled binary surfactant Cahn-Hilliard phase-field model (abbreviated as DCHS) considered in this article, a natural question is how difficult it is to design an "ideal" type scheme. One may think it is not difficult at all because there exist so many effective numerical methods that can handle the phase-field equations (*e.g.*, the Invariant Energy Quadratization (IEQ) method [39,48,53], Scalar Auxiliary Variable (SAV) method [40,49,52,57], convex splitting method [20], etc.), and the "ideal" scheme can be easily and naturally obtained after stacking these methods with any effective numerical method of the Darcy equation.

However, the fact is quite the opposite. As far as the author knows, for the Darcy coupled with the phase-field equations, the only scheme owning the properties of "decoupling, second-order time accuracy, energy stability" (partially "ideal" type scheme due to the lack of linearity) was developed in [21, 22]. The scheme uses the implicit-explicit combination method to deal with the advection and surface tension terms. Using the linear relationship between the pressure gradient and velocity, the fluid velocity in the advection term is formulated by the pressure and surface tension terms, so as to achieve a fully-decoupled scheme (see the details introduced in Rem. 3.9). However, if the same technique developed in [21,22] is applied to the DCHS model, we will quickly find that the fluid velocity in the advection term involves both phase-field variables. This means that although the velocity field can be decoupled from the two Cahn-Hilliard equations, the price to pay is that the two Cahn-Hilliard equations remain coupled. In addition, another disadvantage of this method is that the Cahn-Hilliard equation with variable coefficients must be solved at each time step, which results in a higher computational cost than just solving equations with constant coefficients (see Rem. 3.9).

Therefore, in order to solve the highly complex nonlinear DCHS model, we aim to construct an "ideal" type fully-discrete numerical scheme, where the main challenge that needs to be overcome is how to obtain a decoupling structure and second-order accuracy while keeping the linearity and maintaining the energy stability unconditionally. We achieve such a scheme by assembling several proven methods, including the finite element method for the spatial discretization, projection method for the Darcy equation, the quadratization approach for the nonlinear energy functional, and a new decoupling method to deal with the coupled terms (advection and surface tension). Inspired by the "zero-energy-contribution" property (see Rem. 2.3) satisfied by these coupled terms, the decoupling method is developed by introducing an additional nonlocal variable and designing a special ordinary differential equation (ODE), which consists of the inner product of the coupled terms with some specific functions. This ODE is trivial at the continuous level because all the terms contained in it provide a zero summation. But after discretization, it can help to obtain unconditional energy stability. Meanwhile, the nonlocal variable can decompose each discrete equation into multiple sub-equations that can be solved independently, thereby obtaining a fully-decoupled structure. Besides, the high efficiency of this scheme is also reflected in that not only can all variables be calculated in a decoupled manner, but all equations have constant coefficients at each time step. We also give rigorous proofs of the solvability and unconditional energy stability of the scheme. To demonstrate the stability and accuracy numerically, we further simulate various numerical examples, including the Saffman-Taylor fingering instability caused by the continuously injected radical/uniform flow or rotating Hele-Shaw cell, in which the weakening effects of surfactants on surface tension can be verified by the number of generated fingers.

The rest of this article is organized as follows. We first introduce the DCHS model limited in the Hele-Shaw cell in Section 2, and its law of energy dissipation is derived. In Section 3, we construct a fully-discrete finite element scheme of the "ideal" type, and describe its implementations in detail. Unconditional energy stability and solvability are also proved rigorously. In Section 4, we perform several accuracy/stability tests and implement various simulations on the Saffman-Taylor fingering instability problems to demonstrate the effectiveness of the scheme. In Section 5, some concluding remarks are given finally.

2. GOVERNING SYSTEM

Now, we give a brief introduction of the DCHS system limited to the Hele-Shaw cell. Suppose that Ω is a smooth, open, bounded, connected domain in $\mathbb{R}^d$, $d = 2, 3$. We adopt two phase-field variables $\phi(\boldsymbol{x}, t)$ and $\psi(\boldsymbol{x}, t)$, where ϕ is used to represent the density (or volume fraction) of the two fluids, and ψ is used to represent the local concentration of surfactants, *i.e.*,

$$\phi(\boldsymbol{x},t) = \begin{cases} -1 & \text{fluid I}, \\ 1 & \text{fluid II}, \end{cases} \tag{2.1}$$

with a thin, smooth transition region with a width $O(\epsilon)$. The mixing free energy associated with ϕ and ψ is assumed as follows (see [28, 44, 45, 49, 56]),

$$E_{\text{mix}}(\phi,\psi) = \int_\Omega \left(\lambda_1 (\frac{1}{2}|\nabla\phi|^2 + \frac{1}{\epsilon^2}F(\phi)) + \lambda_2(\frac{\gamma}{2}|\nabla\psi|^2 + \frac{1}{\eta^2}G(\psi)) + W(\phi,\psi) \right) d\boldsymbol{x} \tag{2.2}$$

where

$$\begin{cases} F(\phi) = \frac{1}{4}(\phi^2-1)^2, \ W(\phi,\psi) = -\frac{\theta}{2}\psi|\nabla\phi|^2 + \frac{\zeta}{4}|\nabla\phi|^4, \\ G(\psi) = \alpha_4\psi^4 + \alpha_3\psi^3 + \alpha_2\psi^2 + \alpha\psi, (\alpha_1,\alpha_2,\alpha_3,\alpha_4) = (3.62, -7.25, 7.30, -3.68), \end{cases} \tag{2.3}$$

and $\lambda_1, \lambda_2, \epsilon, \gamma, \eta, \theta, \zeta$ are all positive parameters. The total free energy includes the hydrophilic (gradient)-hydrophobic (double-well) trend of the phase-field variable ϕ where the parameter ϵ represents the width of the binary fluid interface, and the hydrophilicity (gradient)-hydrophobic (quartic polynomial G) trend of the concentration variable ψ where η is a penalty parameter. The last component $W(\phi, \psi)$ includes the coupling item between the surfactant and the fluid interface, where the parameter θ controls the degree of the effect of the surfactant accumulated on the fluid interface, and the ζ term ($\zeta \ll 1$) is used to ensure that the total free energy is bounded from below, see [49, 56].

Remark 2.1. There are many different options for the hydrophobic functional $G(\psi)$. For example, it can be selected as the Flory-Huggins logarithmic type which reads as $G(\psi) = \psi\ln\psi + (1-\psi)\ln(1-\psi)$ (*cf.* [44, 45, 56]), double-well type (*cf.* [25]), or quartic polynomial type given in (2.3) (*cf.* [49]). The last option is used here because it can easily obtain the boundedness property (from below) of the energy potential, which is significant for the well-posedness of the model and the development of numerical algorithms.

Assuming that the fluid motion conforms to the mechanical principles in porous medium, the DCHS model reads as:

$$\phi_t + \nabla\cdot(\mathbf{u}\phi) = M_1\Delta\mu, \tag{2.4}$$

$$\mu = \lambda_1(-\Delta\phi + \frac{1}{\epsilon^2}f(\phi)) + W_\phi, \tag{2.5}$$

$$\psi_t + \nabla\cdot(\mathbf{u}\psi) = M_2\Delta\omega, \tag{2.6}$$

$$\omega = \lambda_2(-\gamma\Delta\psi + \frac{1}{\eta^2}g(\psi)) + W_\psi, \tag{2.7}$$

$$\mathbf{u}_t + \alpha\nu(\phi)\mathbf{u} + \nabla p + \phi\nabla\mu + \psi\nabla\omega = 0, \tag{2.8}$$

$$\nabla\cdot\mathbf{u} = 0, \tag{2.9}$$

where

$$\begin{cases} \mu = \dfrac{\delta E_{\text{mix}}}{\delta \phi}, \omega = \dfrac{\delta E_{\text{mix}}}{\delta \psi}, f(\phi) = F'(\phi) = \phi(\phi^2 - 1), g(\psi) = G'(\psi), \\ W_\phi = \dfrac{\delta W(\phi, \psi)}{\delta \phi} = \theta \nabla \cdot (\psi \nabla \phi) - \zeta \nabla \cdot (|\nabla \phi|^2 \nabla \phi), W_\psi = \dfrac{\delta W(\phi, \psi)}{\delta \psi} = -\dfrac{\theta}{2}|\nabla \phi|^2, \end{cases} \tag{2.10}$$

$\mathbf{u}$ is the dimensionless seepage velocity, τ is a positive parameter, M_1, M_2 are two mobility parameters, α is the dimensionless hydraulic conductivity, $\nu(\phi) = \frac{1}{2}\nu_1(1-\phi) + \frac{1}{2}\nu_2(1+\phi)$ is the fluid viscosity [14], ν_1 and ν_2 are the viscosity for fluid I and II, respectively, p is the pressure. Note that the time derivative of the seepage velocity $\mathbf{u}$ is retained for flows in porous medium, *cf.* [4, 21, 22, 30]. The boundary conditions read as

$$\mathbf{u} \cdot \boldsymbol{n}|_{\partial\Omega} = \partial_{\boldsymbol{n}}\phi|_{\partial\Omega} = \partial_{\boldsymbol{n}}\psi|_{\partial\Omega} = \partial_{\boldsymbol{n}}\mu|_{\partial\Omega} = \partial_{\boldsymbol{n}}\omega|_{\partial\Omega} = 0, \tag{2.11}$$

where $\boldsymbol{n}$ is the unit outward normal on the boundary $\partial\Omega$. Note that the above boundary conditions also implies $\partial_{\boldsymbol{n}} p|_{\partial\Omega} = 0$. It is also possible to assume periodic boundary conditions for all variables. The initial conditions read as

$$(\mathbf{u}, p, \phi, \psi)|_{t=0} = (\mathbf{u}^0, p^0, \phi^0, \psi^0). \tag{2.12}$$

The total mass of local density variable ϕ and concentration variable ψ are conserved over time since

$$\frac{d}{dt}\int_\Omega \phi d\boldsymbol{x} = 0, \ \frac{d}{dt}\int_\Omega \psi d\boldsymbol{x} = 0, \tag{2.13}$$

which can be obtained by integrating (2.4) and (2.6) and using the boundary conditions (2.11).

Some notations are introduced here. We denote the L^2 inner product of any two functions $\phi(\boldsymbol{x})$ and $\psi(\boldsymbol{x})$ is denoted by $(\phi, \psi) = \int_\Omega \phi(\boldsymbol{x})\psi(\boldsymbol{x})d\boldsymbol{x}$, and the L^2 norm of $\phi(\boldsymbol{x})$ is denoted by $\|\phi\|^2 = (\phi, \phi)$. It is easy to see that the entire DCHS system (2.4)–(2.9) holds the law of energy dissipation by performing the standard derivation as follows.

Lemma 2.2. *The following energy law holds for the system* (2.4)*–*(2.9)*:*

$$\frac{d}{dt}E_{\text{tot}}(\phi, \psi, \mathbf{u}) = -M_1\|\nabla \mu\|^2 - M_2\|\nabla \omega\|^2 - \alpha\|\sqrt{\nu(\phi)}\mathbf{u}\|^2, \tag{2.14}$$

where

$$E_{\text{tot}}(\phi, \psi, \mathbf{u}) = E_{\text{mix}}(\phi, \psi) + \frac{1}{2}\int_\Omega |\mathbf{u}|^2 d\boldsymbol{x}. \tag{2.15}$$

Proof. First, we take the inner product of (2.4) with μ, of (2.6) with ω in L^2, and use integration by parts to get

$$(\phi_t, \mu) = -M_1\|\nabla \mu\|^2 - \int_\Omega \nabla \cdot (\mathbf{u}\phi)\mu d\boldsymbol{x}, \tag{2.16}$$

$$(\psi_t, \omega) = -M_2\|\nabla \omega\|^2 - \int_\Omega \nabla \cdot (\mathbf{u}\psi)\omega d\boldsymbol{x}. \tag{2.17}$$

Second, we take the inner product of (2.5) with $-\phi_t$, of (2.7) with $-\psi_t$ in L^2, and use integration by parts to get

$$-(\mu, \phi_t) = -\frac{d}{dt}\int_\Omega \lambda_1(\frac{1}{2}|\nabla \phi|^2 + \frac{1}{\epsilon^2}F(\phi))d\boldsymbol{x} - \int_\Omega W_\phi \phi_t d\boldsymbol{x}, \tag{2.18}$$

$$-(\omega,\psi_t)=-\frac{d}{dt}\int_\Omega \lambda_2(\frac{\gamma}{2}|\nabla\psi|^2+\frac{1}{\eta^2}G(\psi))d\boldsymbol{x}-\int_\Omega W_\psi\psi_t d\boldsymbol{x}. \tag{2.19}$$

Third, we take the inner product of (2.8) with $\mathbf{u}$ in L^2, and use (2.9) to obtain

$$\frac{d}{dt}\int_\Omega \frac{1}{2}|\mathbf{u}|^2 d\boldsymbol{x}+\alpha\|\sqrt{\nu(\phi)}\mathbf{u}\|^2=-\int_\Omega \phi\nabla\mu\cdot\mathbf{u}d\boldsymbol{x}-\int_\Omega \psi\nabla\omega\cdot\mathbf{u}d\boldsymbol{x}. \tag{2.20}$$

Combining the above five equations, we derive the energy law (2.14). □

Remark 2.3. In the process of deriving the energy law (2.14), we find that the four nonlinear terms associated with the advection and surface tensions are cancelled out, namely,

$$\int_\Omega \nabla\cdot(\mathbf{u}\phi)\mu d\boldsymbol{x}+\int_\Omega \phi\nabla\mu\cdot\mathbf{u}d\boldsymbol{x}=0,\quad \int_\Omega \nabla\cdot(\mathbf{u}\psi)\omega d\boldsymbol{x}+\int_\Omega \psi\nabla\omega\cdot\mathbf{u}d\boldsymbol{x}=0. \tag{2.21}$$

These equalities are derived by using the integration by parts and the boundary conditions for $\mathbf{u}$ (periodic or $\mathbf{u}\cdot\boldsymbol{n}|_{\partial\Omega}=0$). These two equalities can be regarded as the contribution of two types of nonlinear terms (advection: $\nabla\cdot(\mathbf{u}\phi)$ and $\nabla\cdot(\mathbf{u}\psi)$, and surface tensions: $\phi\nabla\mu$ and $\psi\nabla\omega$) to the total free energy of the system is zero. These unique "zero-energy-contribution" properties will be used to design decoupling type numerical schemes.

3. NUMERICAL SCHEME

In this section, we aim to construct an "ideal" type fully-discrete finite element scheme to solve the DCHS system (2.4)–(2.9). Some special processing is needed to develop appropriate temporal discretizations for the challenging terms, including the advection, the surface tension, the nonlinear cubic term $f(\phi)$, and the linear coupling between velocity and pressure through the divergence-free condition.

3.1. Reformulated equivalent system and energy law

We introduce a nonlocal variable $Q(t)$ and design an ODE system for it, that reads as:

$$\begin{cases} Q_t=\int_\Omega \Big(-\phi\mathbf{u}\cdot\nabla\mu-\psi\mathbf{u}\cdot\nabla\omega+\phi\nabla\mu\cdot\mathbf{u}+\psi\nabla\omega\cdot\mathbf{u}\Big)d\boldsymbol{x},\\ Q|_{(t=0)}=1. \end{cases} \tag{3.1}$$

It is easy to see that the system (3.1) is the same as a trivial ODE system of $Q_t=0, Q|_{t=0}=1$ with the exact solution of $Q(t)=1$.

We further define a nonlocal variable $U(t)$ as

$$U=\sqrt{\int_\Omega N(\phi,\psi)d\boldsymbol{x}+B}, \tag{3.2}$$

where $N(\phi,\psi)=\lambda_1\frac{F(\phi)}{\epsilon^2}+\lambda_2\frac{G(\psi)}{\eta^2}+W(\phi,\psi)$, B is a constant to guarantee the radicand always be positive. We can always find such a constant B since the nonlocal term in the radicand is always bounded from below. This is because it is easy to see that $-\frac{\theta}{2}\psi|\nabla\phi|^2\geq-\frac{\varsigma}{4}|\nabla\phi|^4-c\psi^2$ for some constant c, and $-c\psi^2$ can be always bounded by the quartic polynomial $G(\psi)$.

We rewrite the original system (2.4)–(2.9) using the new variables Q and U to the following:

$$\phi_t + Q\nabla\cdot(\mathbf{u}\phi) = M_1\Delta\mu, \tag{3.3}$$

$$\mu = -\lambda_1\Delta\phi + HU, \tag{3.4}$$

$$\psi_t + Q\nabla\cdot(\mathbf{u}\psi) = M_2\Delta\omega, \tag{3.5}$$

$$\omega = -\lambda_2\gamma\Delta\psi + RU, \tag{3.6}$$

$$U_t = \frac{1}{2}\int_\Omega (H\phi_t + R\psi_t)d\boldsymbol{x}, \tag{3.7}$$

$$\mathbf{u}_t + \alpha\nu(\phi)\mathbf{u} + \nabla p + Q\phi\nabla\mu + Q\psi\nabla\omega = 0, \tag{3.8}$$

$$\nabla\cdot\mathbf{u} = 0, \tag{3.9}$$

$$Q_t = \int_\Omega \Big(-\phi\mathbf{u}\cdot\nabla\mu - \psi\mathbf{u}\cdot\nabla\omega + \phi\nabla\mu\cdot\mathbf{u} + \psi\nabla\omega\cdot\mathbf{u}\Big)d\boldsymbol{x}, \tag{3.10}$$

where

$$H(\phi,\psi) = \frac{\lambda_1\frac{f(\phi)}{\epsilon^2} + W_\phi}{\sqrt{\int_\Omega N(\phi,\psi)d\boldsymbol{x} + B}}, R(\phi,\psi) = \frac{\lambda_2\frac{g(\psi)}{\eta^2} + W_\psi}{\sqrt{\int_\Omega N(\phi,\psi)d\boldsymbol{x} + B}}. \tag{3.11}$$

The transformed system (3.3)–(3.10) satisfies the following initial conditions,

$$\begin{cases} (\mathbf{u},p,\phi,\psi)|_{t=0} = (\mathbf{u}^0,p^0,\phi^0,\psi^0), Q|_{t=0} = 1, \\ U|_{t=0} = \sqrt{\displaystyle\int_\Omega N(\phi^0,\psi^0)d\boldsymbol{x} + B}. \end{cases} \tag{3.12}$$

Some detailed explanations about the reformulation are given in the remarks below.

Remark 3.1. We multiply the advection terms ($\nabla\cdot(\mathbf{u}\phi)$, $\nabla\cdot(\mathbf{u}\psi)$) and surface tension terms ($\phi\nabla\mu$, $\psi\nabla\omega$) with Q. Since the nonlocal variable $Q(t)$ is equal to 1, the PDE system will not be changed by this modification. Meanwhile, note that the three new equations ((3.4),(3.6),(3.7)) are equivalent to the original equation ((2.5),(2.7)). Therefore, the two PDE systems, (3.3)–(3.10) and (2.4)–(2.9) are equivalent.

Remark 3.2. The mass-conserved property of the two phase-field variables ϕ, ψ remains unchanged in the new system (3.3)–(3.10) noting that the variable Q is nonlocal (*i.e.*, $\int_\Omega Q\nabla\cdot(\mathbf{u}\phi)d\boldsymbol{x} = Q\int_\Omega \nabla\cdot(\mathbf{u}\phi)d\boldsymbol{x}$). By integrating for (3.4) and (3.6) and using integration by parts, we still derive

$$\frac{d}{dt}\int_\Omega \phi d\boldsymbol{x} = 0, \quad \frac{d}{dt}\int_\Omega \psi d\boldsymbol{x} = 0. \tag{3.13}$$

This means that the mass of two fluids and the concentration of the surfactants are still conserved over time.

Lemma 3.3. *The transformed system* (3.3)*–*(3.10) *also follows an energy dissipative law as*

$$\frac{d}{dt}\hat{E}_{\text{tot}}(\phi,\psi,\mathbf{u},Q,U) = -M_1\|\nabla\mu\|^2 - M_2\|\nabla\omega\|^2 - \alpha\|\sqrt{\nu(\phi)}\mathbf{u}\|^2, \tag{3.14}$$

where $\hat{E}_{\text{tot}}(\phi,\psi,\mathbf{u},Q,U) = \int_\Omega \Big(\frac{1}{2}|\mathbf{u}|^2 + \frac{\lambda_1}{2}|\nabla\phi|^2 + \frac{\lambda_2\gamma}{2}|\nabla\psi|^2\Big)d\boldsymbol{x} + |U|^2 + \frac{1}{2}|Q|^2 - B.$

Proof. First, we take the inner product of (3.3) with μ, and of (3.5) with ω in L^2, respectively, and use integration by parts to get

$$(\phi_t,\mu) = -M_1\|\nabla\mu\|^2 + Q\int_\Omega \phi\mathbf{u}\cdot\nabla\mu d\boldsymbol{x}, \tag{3.15}$$

$$(\psi_t,\omega) = -M_2\|\nabla\omega\|^2 + Q\int_\Omega \psi\mathbf{u}\cdot\nabla\omega d\boldsymbol{x}. \tag{3.16}$$

Second, we take the inner product of (3.4) with $-\phi_t$, and of (3.6) with $-\psi_t$ in L^2, respectively, and use integration by parts to get

$$-(\mu, \phi_t) = -\frac{d}{dt}\int_\Omega \frac{\lambda_1}{2}|\nabla\phi|^2 d\boldsymbol{x} - U\int_\Omega H\phi_t d\boldsymbol{x}, \tag{3.17}$$

$$-(\omega, \psi_t) = -\frac{d}{dt}\int_\Omega \frac{\lambda_2\gamma}{2}|\nabla\psi|^2 d\boldsymbol{x} - U\int_\Omega R\psi_t d\boldsymbol{x}. \tag{3.18}$$

By multiplying (3.7) with $2U$, we obtain

$$\frac{d}{dt}|U|^2 = U\int_\Omega H\phi_t d\boldsymbol{x} + U\int_\Omega R\psi_t d\boldsymbol{x}. \tag{3.19}$$

Third, we take the inner product of (3.8) with $\mathbf{u}$ in L^2, and use (3.9) to obtain

$$\frac{d}{dt}\int_\Omega \frac{1}{2}|\mathbf{u}|^2 d\boldsymbol{x} + \alpha\|\sqrt{\nu(\phi)}\mathbf{u}\|^2 = -Q\int_\Omega \phi\nabla\mu\cdot\mathbf{u}d\boldsymbol{x} - Q\int_\Omega \psi\nabla\omega\cdot\mathbf{u}d\boldsymbol{x}. \tag{3.20}$$

By multiplying (3.10) with Q, we obtain

$$\begin{aligned}\frac{d}{dt}\Big(\frac{1}{2}|Q|^2\Big) = &-Q\int_\Omega \phi\mathbf{u}\cdot\nabla\mu d\boldsymbol{x} - Q\int_\Omega \psi\mathbf{u}\cdot\nabla\omega d\boldsymbol{x}\\ &+Q\int_\Omega \phi\nabla\mu\cdot\mathbf{u}d\boldsymbol{x} + Q\int_\Omega \psi\nabla\omega\cdot\mathbf{u}d\boldsymbol{x}.\end{aligned} \tag{3.21}$$

Combining (3.15)–(3.21), we derive the law of energy disspation (3.14), that is now related to the new variables Q, U. □

3.2. Fully-discrete finite element numerical scheme

We develop the fully-discrete finite element scheme for the modified model (3.3)–(3.10) in this section.

We first formulate the PDE system (3.3)–(3.10) to the weak form. Some Hilbert spaces are introduced as follows:

$$\mathbf{X} = L^2(\Omega)^d, L_0^2(\Omega) = \{q\in L^2(\Omega) : \int_\Omega q d\boldsymbol{x} = 0\}, Y = H^1(\Omega), M = H^1(\Omega)\cap L_0^2(\Omega). \tag{3.22}$$

The weak formulation of the system (3.3)–(3.10) reads as: find $(\phi, \mu, \psi, \omega, \mathbf{u}, p) \in Y\times Y\times Y\times Y\times \mathbf{X}\times M$, such that

$$(\phi_t, \Theta) - Q(\mathbf{u}\phi, \nabla\Theta) = -M_1(\nabla\mu, \nabla\Theta) \tag{3.23}$$

$$(\mu, \varphi) = \lambda_1(\nabla\phi, \nabla\varphi) + U(H, \varphi), \tag{3.24}$$

$$(\psi_t, \varpi) - Q(\mathbf{u}\psi, \nabla\varpi) = -M_2(\nabla\omega, \nabla\varpi), \tag{3.25}$$

$$(\omega, \Psi) = \lambda_2\gamma(\nabla\psi, \nabla\Psi) + U(R, \Psi), \tag{3.26}$$

$$U_t = \frac{1}{2}\int_\Omega (H\phi_t + R\psi_t) d\boldsymbol{x}, \tag{3.27}$$

$$(\mathbf{u}_t, \boldsymbol{v}) + \alpha(\nu(\phi)\mathbf{u}, \boldsymbol{v}) + (\nabla p, \boldsymbol{v}) + Q(\phi\nabla\mu, \boldsymbol{v}) + Q(\psi\nabla\omega, \boldsymbol{v}) = 0, \tag{3.28}$$

$$(\mathbf{u}, \nabla q) = 0, \tag{3.29}$$

$$Q_t = \int_\Omega \Big(-\phi\mathbf{u}\cdot\nabla\mu - \psi\mathbf{u}\cdot\nabla\omega + \phi\nabla\mu\cdot\mathbf{u} + \psi\nabla\omega\cdot\mathbf{u}\Big) d\boldsymbol{x}, \tag{3.30}$$

for $(\varphi, \Theta, \Psi, \varpi, \boldsymbol{v}, q) \in Y \times Y \times Y \times Y \times \mathbf{X} \times M$.

Before the numerical scheme, we introduce a few finite dimensional discrete subspaces. Assuming that the polygonal/polyhedral domain Ω is discretized by a conforming and shape regular triangulation/tetrahedron mesh $\mathcal{T}_h$ that is composed by open disjoint elements K such that $\bar{\Omega} = \bigcup_{K \in \mathcal{T}_h} \bar{K}$. We use $\mathcal{P}_k$ to denote the space of polynomials of total degree at most k ($k \geq 1$) and define the following finite element spaces:

$$\begin{aligned} \boldsymbol{X}_h &= \left\{\boldsymbol{v} \in L^2(\Omega)^d : \boldsymbol{v}|_K \in \mathcal{P}_{l-1}(K)^d, \forall K \in \mathcal{T}_h\right\}, \\ M_h &= \left\{p \in H^1(\Omega) \cap L_0^2(\Omega) : p|_K \in \mathcal{P}_l(K)\right\}, \\ Y_h &= \left\{X \in C^0(\Omega) : X|_K \in \mathcal{P}_\ell(K), \forall K \in \mathcal{T}_h\right\}. \end{aligned} \tag{3.31}$$

Hence $\boldsymbol{X}_h \subset L^2(\Omega)^d, M_h \subset L_0^2(\Omega), Y_h \subset H^1(\Omega)$.

Using the second-order backward differentiation formula for the time derivative, we construct the fully discrete scheme to solve the system (3.23)–(3.30) as follows: find $\phi_h^{n+1} \in Y_h, \mu_h^{n+1} \in Y_h, \psi_h^{n+1} \in Y_h, \omega_h^{n+1} \in Y_h, \tilde{\mathbf{u}}_h^{n+1} \in \boldsymbol{X}_h, \mathbf{u}_h^{n+1} \in \boldsymbol{X}_h, p_h^{n+1} \in M_h$, and two nonlocal scalars U^{n+1}, Q^{n+1} such that

$$\left(\frac{a\phi_h^{n+1} - b\phi_h^n + c\phi_h^{n-1}}{2\delta t}, \Theta_h\right) - Q^{n+1}(\mathbf{u}_h^*\phi_h^*, \nabla\Theta_h) = -M_1(\nabla\mu_h^{n+1}, \nabla\Theta_h), \tag{3.32}$$

$$(\mu_h^{n+1}, \varphi_h) = \lambda_1(\nabla\phi_h^{n+1}, \nabla\varphi_h) + U^{n+1}(H^*, \varphi_h) + \frac{S_1}{\epsilon^2}(\phi_h^{n+1} - \phi_h^*, \varphi_h), \tag{3.33}$$

$$\left(\frac{a\psi_h^{n+1} - b\psi_h^n + c\psi_h^{n-1}}{2\delta t}, \varpi_h\right) - Q^{n+1}(\mathbf{u}_h^*\psi_h^*, \nabla\varpi_h) = -M_2(\nabla\omega_h^{n+1}, \nabla\varpi_h), \tag{3.34}$$

$$(\omega_h^{n+1}, \Psi_h) = \lambda_2\gamma(\nabla\omega_h^{n+1}, \nabla\Psi_h) + U^{n+1}(R^*, \Psi_h) + \frac{S_2}{\eta^2}(\psi_h^{n+1} - \psi_h^*, \Psi_h), \tag{3.35}$$

$$\begin{aligned} aU^{n+1} - bU^n + cU^{n-1} = \frac{1}{2}\int_\Omega \Big(& H^*(a\phi_h^{n+1} - b\phi_h^n + c\phi_h^{n-1}) \\ &+ R^*(a\psi_h^{n+1} - b\psi_h^n + c\psi_h^{n-1})\Big) d\boldsymbol{x}, \end{aligned} \tag{3.36}$$

$$\begin{aligned} \left(\frac{a\tilde{\mathbf{u}}_h^{n+1} - b\mathbf{u}_h^n + c\mathbf{u}_h^{n-1}}{2\delta t}, \boldsymbol{v}_h\right) &+ \alpha(\nu(\hat{\phi}_h^*)\tilde{\mathbf{u}}_h^{n+1}, \boldsymbol{v}_h) + (\nabla p_h^n, \boldsymbol{v}_h) \\ &+ Q^{n+1}(\phi_h^*\nabla\mu_h^*, \boldsymbol{v}_h) + Q^{n+1}(\psi_h^*\nabla\omega_h^*, \boldsymbol{v}_h) = 0, \end{aligned} \tag{3.37}$$

$$\begin{aligned} \frac{aQ^{n+1} - bQ^n + cQ^{n-1}}{2\delta t} = \int_\Omega \Big(& -\phi_h^*\mathbf{u}_h^* \cdot \nabla\mu_h^{n+1} - \psi_h^*\mathbf{u}_h^* \cdot \nabla\omega_h^{n+1} \\ &+ \phi_h^*\nabla\mu_h^* \cdot \tilde{\mathbf{u}}_h^{n+1} + \psi_h^*\nabla\omega_h^* \cdot \tilde{\mathbf{u}}_h^{n+1}\Big) d\boldsymbol{x}, \end{aligned} \tag{3.38}$$

$$(\nabla(p_h^{n+1} - p_h^n), \nabla q_h) = \frac{a}{2\delta t}(\tilde{\mathbf{u}}_h^{n+1}, \nabla q_h), \tag{3.39}$$

$$\mathbf{u}_h^{n+1} = \tilde{\mathbf{u}}_h^{n+1} - \frac{2\delta t}{a}(\nabla p_h^{n+1} - \nabla p_h^n), \tag{3.40}$$

for all $\Theta_h \in Y_h, \varphi_h \in Y_h, \varpi_h \in Y_h, \Psi_h \in Y_h, \boldsymbol{v}_h \in \boldsymbol{X}_h, q_h \in M_h$, where

$$\begin{aligned} & a = 3, b = 4, c = 1, \mathbf{u}_h^* = 2\mathbf{u}_h^n - \mathbf{u}_h^{n-1}, \phi_h^* = 2\phi_h^n - \phi_h^{n-1}, \\ & \mu_h^* = 2\mu_h^n - \mu_h^{n-1}, \psi_h^* = 2\psi_h^n - \psi_h^{n-1}, \omega_h^* = 2\omega_h^n - \omega_h^{n-1}, \\ & H^* = H(\phi_h^*), R^* = R(\psi_h^*), \hat{\phi} = \begin{cases} \phi, & |\phi| < 1, \\ \operatorname{sign}(\phi), & |\phi| > 1, \end{cases} \end{aligned} \tag{3.41}$$

and S_1 and S_2 are two positive stabilization parameters.

Several remarks are in order.

Remark 3.4. The computations of the second-order scheme (3.32)–(3.40) require all values of $t = t^1$. In practice, we can obtain these values by constructing a similar first-order scheme based on the backward Euler method as long as we set $a = b = 2, c = 0, r^* = r^0, \forall r$. Meanwhile, similar to the continuous case, the mass-conserved property of ϕ_h^{n+1} and ψ_h^{n+1} still holds, which can be proved by taking $\Theta_h = \varpi_h = 1$ in (3.32) and (3.34). We can derive $\int_\Omega \phi_h^{n+1} d\boldsymbol{x} = \int_\Omega \frac{b\phi_h^n - c\phi_h^{n-1}}{a} d\boldsymbol{x}$ and $\int_\Omega \psi_h^{n+1} d\boldsymbol{x} = \int_\Omega \frac{b\psi_h^n - c\psi_h^{n-1}}{a} d\boldsymbol{x}$. By using the math induction, it is easy to obtain $\int_\Omega \phi_h^{n+1} d\boldsymbol{x} = \int_\Omega \phi_h^n d\boldsymbol{x} = \cdots = \int_\Omega \phi_h^0 d\boldsymbol{x}$ and $\int_\Omega \psi_h^{n+1} d\boldsymbol{x} = \int_\Omega \psi_h^n d\boldsymbol{x} = \cdots = \int_\Omega \psi_h^0 d\boldsymbol{x}$.

Remark 3.5. A second-order pressure-correction scheme is used to decouple the computation of the pressure from that of the velocity. $\tilde{\mathbf{u}}^{n+1}$ is the intermediate velocity and $\mathbf{u}^{n+1}$ is the final velocity field that satisfies the divergence free condition. $\mathbf{u}_h^{n+1}$ satisfies the discrete divergence free condition that can be deduced by taking the L^2 inner product of (3.40) with ∇q_h where $q_h \in M_h$, that is

$$(\mathbf{u}_h^{n+1}, \nabla q_h) = (\tilde{\mathbf{u}}_h^{n+1}, \nabla q_h) - \frac{2\delta t}{a}(\nabla(p_h^{n+1} - p_h^n), \nabla q_h) = 0, \tag{3.42}$$

where (3.39) is used.

Remark 3.6. When the system has very high stiffness issues caused by the model parameters or other conditions, while some numerical methods are formally unconditionally energy stable, but exceedingly small time steps are needed to achieve reasonable accuracy, see the stabilized-IEQ/SAV methods in [9, 39, 47, 55]. To fix such an inherent deficiency, a commonly used effective way is to add one or more extra linear stabilization terms with the corresponding temporal order (*cf.* the second-order term associated with S_1 in (3.33) and S_2 in (3.35)). The scale of the splitting errors caused by this term are about $\frac{S_1}{\epsilon^2}\delta t^2 \partial_{tt}\phi(\cdot)$ and $\frac{S_2}{\eta^2}\delta t^2 \partial_{tt}\psi(\cdot)$, which are actually consistent with the error caused by the second-order extrapolated nonlinear term $f(\phi)$ and $g(\psi)$. In Section 4, we present numerical evidence to show that this stabilizer is effective to improve the energy stability while using large time steps in Figure 3. Similar linear stabilization techniques had been widely used in the numerical scheme for solving the phase-field type models, *e.g.*, the methods of linear stabilization, IEQ, SAV, convex-splitting methods, etc., see [8, 9, 11, 38, 39, 47, 50, 51, 54, 55].

Remark 3.7. Note that $\frac{1}{\delta t}(E^{n+1} - E^n)$ is actually a temporal second-order approximation of the term $\frac{d}{dt}\hat{E}_{\text{tot}}(\phi, \psi, \mathbf{u}, Q, U)$ at $t = t^{n+1}$. Since for any smooth variable ψ with time, we always have the following heuristic approximations as

$$\begin{aligned} &\frac{\|\psi^{n+1}\|^2 + \|2\psi^{n+1} - \psi^n\|^2}{2\delta t} - \frac{\|\psi^n\|^2 + \|2\psi^n - \psi^{n-1}\|^2}{2\delta t} \\ &\qquad\cong \frac{\|\psi^{n+2}\|^2 - \|\psi^n\|^2}{2\delta t} + O(\delta t^2) \cong \frac{d}{dt}\|\psi(t^{n+1})\|^2 + O(\delta t^2). \end{aligned} \tag{3.43}$$

We now show that the scheme (3.32)–(3.40) is unconditionally energy stable. We will use the following three identities repeatedly:

$$2(a - b, a) = |a|^2 - |b|^2 + |a - b|^2, \tag{3.44}$$

$$2(3a - 4b + c)a = |a|^2 - |b|^2 + |2a - b|^2 - |2b - c|^2 + |a - 2b + c|^2, \tag{3.45}$$

$$(3a - 4b + c)(a - 2b + c) = |a - b|^2 - |b - c|^2 + 2|a - 2b + c|^2. \tag{3.46}$$

Theorem 3.8. *The following discrete energy dissipation law holds for the fully-discrete scheme (3.32)–(3.40) that reads as*

$$\frac{1}{\delta t}(E_h^{n+1} - E_h^n) \le -\alpha\|\sqrt{\nu(\hat{\phi}_h^*)}\mathbf{u}_h^{n+1}\|^2 - M_1\|\nabla\mu_h^{n+1}\|^2 - M_2\|\nabla\omega_h^{n+1}\|^2 \le 0, \tag{3.47}$$

where E_h^{n+1} *is defined as*

$$\begin{aligned}E_h^{n+1} =&\frac{1}{2}\Big(\frac{1}{2}\|\mathbf{u}_h^{n+1}\|^2+\frac{1}{2}\|2\mathbf{u}_h^{n+1}-\mathbf{u}_h^n\|^2\Big)+\frac{\lambda_1}{2}(\frac{1}{2}\|\nabla\phi_h^{n+1}\|^2+\frac{1}{2}\|2\nabla\phi_h^{n+1}-\nabla\phi_h^n\|^2)\\&+\frac{\lambda_2\gamma}{2}(\frac{1}{2}\|\nabla\psi_h^{n+1}\|^2+\frac{1}{2}\|2\nabla\psi_h^{n+1}-\nabla\psi_h^n\|^2)\\&+(\frac{1}{2}|U^{n+1}|^2+\frac{1}{2}|2U^{n+1}-U^n|^2)+\frac{1}{2}(\frac{1}{2}|Q^{n+1}|^2+\frac{1}{2}|2Q^{n+1}-Q^n|^2)\\&+\frac{\delta t^2}{3}\|\nabla p_h^{n+1}\|^2+\frac{S_1}{2\epsilon^2}\|\phi_h^{n+1}-\phi_h^n\|^2+\frac{S_2}{2\eta^2}\|\psi_h^{n+1}-\psi_h^n\|^2-B.\end{aligned}\tag{3.48}$$

Proof. Taking $\boldsymbol{v}_h=2\delta t\tilde{\mathbf{u}}_h^{n+1}$ in (3.37), we obtain

$$\begin{aligned}&(3\tilde{\mathbf{u}}_h^{n+1}-4\mathbf{u}_h^n+\mathbf{u}_h^{n-1},\tilde{\mathbf{u}}_h^{n+1})+2\delta t\alpha\|\sqrt{\nu(\hat{\phi}_h^*)}\tilde{\mathbf{u}}_h^{n+1}\|^2+2\delta t(\nabla p_h^n,\tilde{\mathbf{u}}_h^{n+1})\\&\quad+2\delta tQ^{n+1}\int_\Omega\phi_h^*\nabla\mu_h^*\cdot\tilde{\mathbf{u}}_h^{n+1}d\boldsymbol{x}+2\delta tQ^{n+1}\int_\Omega\psi_h^*\nabla\omega_h^*\cdot\tilde{\mathbf{u}}_h^{n+1}d\boldsymbol{x}=0,\end{aligned}\tag{3.49}$$

where we use $\nu(\hat{\phi}_h^*)\geq\min(\nu_1,\nu_2)>0$ from (3.41).

We rewrite (3.40) as

$$\tilde{\mathbf{u}}_h^{n+1}-\mathbf{u}_h^{n+1}=\frac{2\delta t}{3}\nabla(p_h^{n+1}-p_h^n).\tag{3.50}$$

Taking the L^2 inner product of the above equality with $\mathbf{u}_h^{n+1}$, we derive

$$(\tilde{\mathbf{u}}_h^{n+1}-\mathbf{u}_h^{n+1},\mathbf{u}_h^{n+1})=\frac{2\delta t}{3}(\nabla(p_h^{n+1}-p_h^n),\boldsymbol{u}^{n+1})=0,\tag{3.51}$$

and

$$\begin{aligned}&(3\mathbf{u}_h^{n+1}-4\mathbf{u}_h^n+\mathbf{u}_h^{n-1},\tilde{\mathbf{u}}_h^{n+1}-\mathbf{u}_h^{n+1})\\&\quad=(3\mathbf{u}_h^{n+1}-4\mathbf{u}_h^n+\mathbf{u}_h^{n-1},\frac{2\delta t}{3}\nabla(p_h^{n+1}-p_h^n))=0,\end{aligned}\tag{3.52}$$

where (3.42) is used. By using (3.51) and (3.52), we deduce

$$\begin{aligned}(3\tilde{\mathbf{u}}_h^{n+1}&-4\mathbf{u}_h^n+\mathbf{u}_h^{n-1},\tilde{\mathbf{u}}_h^{n+1})\\&=\big(3\tilde{\mathbf{u}}_h^{n+1}-3\mathbf{u}_h^{n+1},\tilde{\mathbf{u}}_h^{n+1}\big)+\big(3\mathbf{u}_h^{n+1}-4\mathbf{u}_h^n+\mathbf{u}_h^{n-1},\tilde{\mathbf{u}}_h^{n+1}\big)\\&=\big(3\tilde{\mathbf{u}}_h^{n+1}-3\mathbf{u}_h^{n+1},\tilde{\mathbf{u}}_h^{n+1}+\mathbf{u}_h^{n+1}\big)+\big(3\mathbf{u}_h^{n+1}-4\mathbf{u}_h^n+\mathbf{u}_h^{n-1},\mathbf{u}_h^{n+1}\big)\\&=\frac{1}{2}(\|\mathbf{u}_h^{n+1}\|^2-\|\mathbf{u}_h^n\|^2+\|2\mathbf{u}_h^{n+1}-\mathbf{u}_h^n\|^2-\|2\mathbf{u}_h^n-\mathbf{u}_h^{n-1}\|^2+\|\mathbf{u}_h^{n+1}-2\mathbf{u}_h^n+\mathbf{u}_h^{n-1}\|^2)\\&\quad+3\|\tilde{\mathbf{u}}_h^{n+1}\|^2-3\|\mathbf{u}_h^{n+1}\|^2.\end{aligned}\tag{3.53}$$

We rewrite (3.40) as

$$\mathbf{u}_h^{n+1}+\frac{2}{3}\delta t\nabla p_h^{n+1}=\tilde{\mathbf{u}}_h^{n+1}+\frac{2}{3}\delta t\nabla p_h^n.$$

Taking the L^2 inner product of the above equation with itself and multiply the result with $\frac{3}{2}$, we derive

$$2\delta t(\tilde{\mathbf{u}}_h^{n+1},\nabla p_h^n)=\frac{3}{2}\|\mathbf{u}_h^{n+1}\|^2-\frac{3}{2}\|\tilde{\mathbf{u}}_h^{n+1}\|^2+\frac{2\delta t^2}{3}\|\nabla p_h^{n+1}\|^2-\frac{2\delta t^2}{3}\|\nabla p_h^n\|^2.\tag{3.54}$$

We rewrite (3.40) as

$$\mathbf{u}_h^{n+1}-\tilde{\mathbf{u}}_h^{n+1}=-\frac{2}{3}\delta t\nabla p_h^{n+1}+\frac{2}{3}\delta t\nabla p_h^{n}. \tag{3.55}$$

By taking the L^2 inner product of the above equation with $3\mathbf{u}_h^{n+1}$, using (3.42) and (3.44), we obtain

$$\frac{3}{2}\|\mathbf{u}_h^{n+1}-\tilde{\mathbf{u}}_h^{n+1}\|^2=\frac{3}{2}\|\tilde{\mathbf{u}}_h^{n+1}\|^2-\frac{3}{2}\|\mathbf{u}_h^{n+1}\|^2. \tag{3.56}$$

By combining (3.49), (3.53), (3.54) and (3.56), we derive

$$\begin{aligned}&\frac{1}{2}(\|\mathbf{u}_h^{n+1}\|^2-\|\mathbf{u}_h^{n}\|^2+\|2\mathbf{u}_h^{n+1}-\mathbf{u}_h^{n}\|^2-\|2\mathbf{u}_h^{n}-\mathbf{u}_h^{n-1}\|^2+\|\mathbf{u}_h^{n+1}-2\mathbf{u}_h^{n}+\mathbf{u}_h^{n-1}\|^2)\\&\qquad+\frac{3}{2}\|\mathbf{u}_h^{n+1}-\tilde{\mathbf{u}}_h^{n+1}\|^2+2\alpha\delta t\|\sqrt{\nu(\hat{\phi}_h^*)}\tilde{\mathbf{u}}_h^{n+1}\|^2+\frac{2\delta t^2}{3}\|\nabla p_h^{n+1}\|^2-\frac{2\delta t^2}{3}\|\nabla p_h^{n}\|^2\\&\qquad+2\delta tQ^{n+1}\int_\Omega\phi_h^*\nabla\mu_h^*\cdot\tilde{\mathbf{u}}_h^{n+1}d\boldsymbol{x}+2\delta tQ^{n+1}\int_\Omega\psi_h^*\nabla\omega_h^*\cdot\tilde{\mathbf{u}}_h^{n+1}d\boldsymbol{x}=0.\end{aligned} \tag{3.57}$$

Taking $\Theta_h=2\delta t\mu_h^{n+1}$ in (3.32) and $\varpi_h=2\delta t\omega_h^{n+1}$ in (3.34), we derive

$$(3\phi_h^{n+1}-4\phi_h^{n}+\phi_h^{n-1},\mu_h^{n+1})-2\delta tQ^{n+1}\int_\Omega\phi_h^*\mathbf{u}_h^*\cdot\nabla\mu_h^{n+1}d\boldsymbol{x}+2\delta tM_1\|\nabla\mu_h^{n+1}\|^2=0, \tag{3.58}$$

and

$$(3\psi_h^{n+1}-4\psi_h^{n}+\psi_h^{n-1},\omega_h^{n+1})-2\delta tQ^{n+1}\int_\Omega\psi_h^*\mathbf{u}_h^*\cdot\nabla\omega_h^{n+1}d\boldsymbol{x}+2\delta tM_2\|\nabla\omega_h^{n+1}\|^2=0. \tag{3.59}$$

Taking $\varphi_h=-(3\phi_h^{n+1}-4\phi_h^{n}+\phi_h^{n-1})$ in (3.33) and $\Psi_h=-(3\psi_h^{n+1}-4\psi_h^{n}+\psi_h^{n-1})$ in (3.35), we find

$$\begin{aligned}&-(\mu_h^{n+1},3\phi_h^{n+1}-4\phi_h^{n}+\phi_h^{n-1})+\lambda_1(\nabla\phi_h^{n+1},\nabla(3\phi_h^{n+1}-4\phi_h^{n}+\phi_h^{n-1}))\\&\quad+U^{n+1}\int_\Omega H^*(3\phi_h^{n+1}-4\phi_h^{n}+\phi_h^{n-1})d\boldsymbol{x}+\frac{S_1}{\epsilon^2}(\phi_h^{n+1}-\phi_h^*,3\phi_h^{n+1}-4\phi_h^{n}+\phi_h^{n-1})=0,\end{aligned} \tag{3.60}$$

and

$$\begin{aligned}&-(\omega_h^{n+1},3\psi_h^{n+1}-4\psi_h^{n}+\psi_h^{n-1})+\lambda_2\gamma(\nabla\psi_h^{n+1},\nabla(3\psi_h^{n+1}-4\psi_h^{n}+\psi_h^{n-1}))\\&\quad+U^{n+1}\int_\Omega R^*(3\psi_h^{n+1}-4\psi_h^{n}+\psi_h^{n-1})d\boldsymbol{x}+\frac{S_2}{\eta^2}(\psi_h^{n+1}-\psi_h^*,3\psi_h^{n+1}-4\psi_h^{n}+\psi_h^{n-1})=0.\end{aligned} \tag{3.61}$$

We multiply (3.36) with $2U^{n+1}$ to obtain

$$\begin{aligned}&|U^{n+1}|^2-|U^n|^2+|2U^{n+1}-U^n|^2-|2U^n-U^{n-1}|^2+|U^{n+1}-2U^n+U^{n-1}|^2\\&\quad=U^{n+1}\left(\int_\Omega H^*(3\phi_h^{n+1}-4\phi_h^{n}+\phi_h^{n-1})d\boldsymbol{x}+\int_\Omega R^*(3\psi_h^{n+1}-4\psi_h^{n}+\psi_h^{n-1})d\boldsymbol{x}\right),\end{aligned} \tag{3.62}$$

where (3.45) is used.

By multiplying (3.38) with $2\delta tQ^{n+1}$ and using (3.45), we obtain

$$\begin{aligned}&\frac{1}{2}\Big(|Q^{n+1}|^2-|Q^n|^2+|2Q^{n+1}-Q^n|^2-|2Q^n-Q^{n-1}|^2+|Q^{n+1}-2Q^n+Q^{n-1}|^2\Big)\\&=2\delta tQ^{n+1}\int_\Omega\Big(-\phi_h^*\mathbf{u}_h^*\cdot\nabla\mu_h^{n+1}-\psi_h^*\mathbf{u}_h^*\cdot\nabla\omega_h^{n+1}\Big)d\boldsymbol{x}\\&\quad+2\delta tQ^{n+1}\int_\Omega\Big(\phi_h^*\nabla\mu_h^*\cdot\tilde{\mathbf{u}}_h^{n+1}+\psi_h^*\nabla\omega_h^*\cdot\tilde{\mathbf{u}}_h^{n+1}\Big)d\boldsymbol{x}.\end{aligned} \tag{3.63}$$

Hence, by combining (3.57)–(3.63) and using (3.45), (3.46), we arrive at

$$\begin{aligned}
&\frac{1}{2}(\|\mathbf{u}_h^{n+1}\|^2-\|\mathbf{u}_h^n\|^2+\|2\mathbf{u}_h^{n+1}-\mathbf{u}_h^n\|^2-\|2\mathbf{u}_h^n-\mathbf{u}_h^{n-1}\|^2)+\frac{2\delta t^2}{3}(\|\nabla p_h^{n+1}\|^2-\|\nabla p_h^n\|^2)\\
&\quad+\frac{\lambda_1}{2}(\|\nabla\phi_h^{n+1}\|^2-\|\nabla\phi_h^n\|^2+\|\nabla(2\phi_h^{n+1}-\phi_h^n)\|^2-\|\nabla(2\phi_h^n-\phi_h^{n-1})\|^2)\\
&\quad+\frac{\lambda_2\gamma}{2}(\|\nabla\psi_h^{n+1}\|^2-\|\nabla\psi_h^n\|^2+\|\nabla(2\psi_h^{n+1}-\psi_h^n)\|^2-\|\nabla(2\psi_h^n-\psi_h^{n-1})\|^2)\\
&\quad+(|U^{n+1}|^2-|U^n|^2+|2U^{n+1}-U^n|^2-|2U^n-U^{n-1}|^2)\\
&\quad+\frac{1}{2}(|Q^{n+1}|^2-|Q^n|^2+|2Q^{n+1}-Q^n|^2-|2Q^n-Q^{n-1}|^2)\\
&\quad+\frac{S_1}{\epsilon^2}(\|\phi_h^{n+1}-\phi_h^n\|^2-\|\phi_h^n-\phi_h^{n-1}\|^2)+\frac{S_2}{\eta^2}(\|\psi_h^{n+1}-\psi_h^n\|^2-\|\psi_h^n-\psi_h^{n-1}\|^2)\\
&\quad+\Big\{\frac{1}{2}\|\mathbf{u}_h^{n+1}-2\mathbf{u}_h^n+\mathbf{u}_h^{n-1}\|^2+\frac{3}{2}\|\mathbf{u}_h^{n+1}-\tilde{\mathbf{u}}_h^{n+1}\|^2\\
&\qquad+\frac{\lambda_1}{2}\|\nabla(\phi_h^{n+1}-2\phi_h^n+\phi_h^{n-1})\|^2+\frac{\lambda_2\gamma}{2}\|\nabla(\psi_h^{n+1}-2\psi_h^n+\psi_h^{n-1})\|^2\\
&\qquad+\frac{2S_1}{\epsilon^2}\|\phi_h^{n+1}-2\phi_h^n+\phi_h^{n-1}\|^2+\frac{2S_2}{\eta^2}\|\psi_h^{n+1}-2\psi_h^n+\psi_h^{n-1}\|^2\\
&\qquad+|U^{n+1}-2U^n+U^{n-1}|^2+\frac{1}{2}|Q^{n+1}-2Q^n+Q^{n-1}|^2\Big\}\\
&\quad=-2\delta t\alpha\|\sqrt{\nu(\hat{\phi}_h^*)}\tilde{\mathbf{u}}_h^{n+1}\|^2-2\delta tM_1\|\nabla\mu_h^{n+1}\|^2-2\delta tM_2\|\nabla\omega_h^{n+1}\|^2.
\end{aligned}\tag{3.64}$$

Finally, by dropping the positive terms in { } of (3.64), we obtain (3.47). □

3.3. Decoupled implementation

In this subsection, we develop the decoupled implementation process for the scheme (3.32)–(3.40) in which we make full use of the nonlocal property of the auxiliary variable Q.

Step 1:, we split $\phi_h^{n+1},\mu_h^{n+1},\psi_h^{n+1},\omega_h^{n+1},U^{n+1}$ into a linear combination form in terms of Q^{n+1}, namely,

$$\begin{cases}\phi_h^{n+1}=\phi_{1h}^{n+1}+Q^{n+1}\phi_{2h}^{n+1},\mu_h^{n+1}=\mu_{1h}^{n+1}+Q^{n+1}\mu_{2h}^{n+1},\\ \psi_h^{n+1}=\psi_{1h}^{n+1}+Q^{n+1}\psi_{2h}^{n+1},\omega_h^{n+1}=\omega_{1h}^{n+1}+Q^{n+1}\omega_{2h}^{n+1},\\ U^{n+1}=U_1^{n+1}+Q^{n+1}U_2^{n+1}.\end{cases}\tag{3.65}$$

We solve $\phi_{ih}^{n+1},\mu_{ih}^{n+1},\psi_{ih}^{n+1},\omega_{ih}^{n+1}$ for $i=1,2$, as follows.

Using (3.65) and according to Q^{n+1}, the system (3.32)–(3.35) can be split into the following four subsystems:

$$\begin{cases}\left(\dfrac{a}{2M_1\delta t}\phi_{1h}^{n+1},\Theta_h\right)=-(\nabla\mu_{1h}^{n+1},\nabla\Theta_h)+(\dfrac{b\phi_h^n-c\phi_h^{n-1}}{2M_1\delta t},\Theta_h),\\ (\mu_{1h}^{n+1},\varphi_h)=\lambda_1(\nabla\phi_{1h}^{n+1},\nabla\varphi_h)+(H^*,\varphi_h)U_1^{n+1}+\dfrac{S_1}{\epsilon^2}(\phi_{1h}^{n+1}-\phi_h^*,\varphi_h),\end{cases}\tag{3.66}$$

$$\begin{cases}\left(\dfrac{a}{2M_1\delta t}\phi_{2h}^{n+1},\Theta_h\right)=-(\nabla\mu_{2h}^{n+1},\nabla\Theta_h)+\dfrac{1}{M_1}(\mathbf{u}_h^*\phi_h^*,\nabla\Theta_h),\\ (\mu_{2h}^{n+1},\varphi_h)=\lambda_1(\nabla\phi_{2h}^{n+1},\nabla\varphi_h)+(H^*,\varphi_h)U_2^{n+1}+\dfrac{S_1}{\epsilon^2}(\phi_{2h}^{n+1},\varphi_h),\end{cases}\tag{3.67}$$

$$\begin{cases} \left(\dfrac{a}{2M_2\delta t}\psi_{1h}^{n+1}, \varpi_h\right) = -(\nabla\omega_{1h}^{n+1}, \nabla\varpi_h) + (\dfrac{b\psi_h^n - c\psi_h^{n-1}}{2M_2\delta t}, \varpi_h), \\ (\omega_{1h}^{n+1}, \Psi_h) = \lambda_2\gamma(\nabla\psi_{1h}^{n+1}, \nabla\Psi_h) + (R^*, \Psi_h)U_1^{n+1} + \dfrac{S_2}{\eta^2}(\psi_{1h}^{n+1} - \psi_h^*, \Psi_h), \end{cases} \tag{3.68}$$

and

$$\begin{cases} \left(\dfrac{a}{2M_2\delta t}\psi_{2h}^{n+1}, \varpi_h\right) = -(\nabla\omega_{2h}^{n+1}, \nabla\varpi_h) + \dfrac{1}{M_2}(\mathbf{u}_h^*\psi_h^*, \nabla\varpi_h), \\ (\omega_2^{n+1}, \Psi_h) = \lambda_2\gamma(\nabla\psi_{2h}^{n+1}, \nabla\Psi_h) + (R^*, \psi_h)U_2^{n+1} + \dfrac{S_2}{\eta^2}(\psi_{2h}^{n+1}, \Psi_h). \end{cases} \tag{3.69}$$

We continue to split $\phi_{ih}^{n+1}, \mu_{ih}^{n+1}, \psi_{ih}^{n+1}, \omega_{ih}^{n+1}$ for $i = 1, 2$ using the nonlocal variables U_1^{n+1} and U_2^{n+1}. Namely, for $i = 1, 2$, we formulate $\phi_{ih}^{n+1}, \mu_{ih}^{n+1}, \psi_{ih}^{n+1}, \omega_{ih}^{n+1}$ as

$$\begin{cases} \phi_{ih}^{n+1} = \phi_{i1h}^{n+1} + U_i^{n+1}\phi_{i2h}^{n+1}, \mu_{ih}^{n+1} = \mu_{i1h}^{n+1} + U_i^{n+1}\mu_{i2h}^{n+1}, \\ \psi_{ih}^{n+1} = \psi_{i1h}^{n+1} + U_i^{n+1}\psi_{i2h}^{n+1}, \omega_{ih}^{n+1} = \omega_{i1h}^{n+1} + U_i^{n+1}\omega_{i2h}^{n+1}. \end{cases} \tag{3.70}$$

Using (3.70), we replace $\phi_{ih}^{n+1}, \mu_{ih}^{n+1}, \psi_{ih}^{n+1}, \omega_{ih}^{n+1}$ in the four subsystems (3.66)–(3.69), and decompose the obtained equations according to U_1^{n+1} and U_2^{n+1} to the following eight sub-systems:

$$\begin{cases} \dfrac{a}{2M_1\delta t}(\phi_{i1h}^{n+1}, \Theta_h) = -(\nabla\mu_{i1h}^{n+1}, \nabla\Theta_h) + G_{i1}, \\ (\mu_{i1h}^{n+1}, \varphi_h) = \lambda_1(\nabla\phi_{i1h}^{n+1}, \nabla\varphi_h) + \dfrac{S_1}{\epsilon^2}(\phi_{i1h}^{n+1}, \varphi_h), i = 1, 2, \end{cases} \tag{3.71}$$

$$\begin{cases} \dfrac{a}{2M_1\delta t}(\phi_{i2h}^{n+1}, \Theta_h) = -(\nabla\mu_{i2h}^{n+1}, \nabla\Theta_h) + G_{i2}, \\ (\mu_{i2h}^{n+1}, \varphi_h) = \lambda_1(\nabla\phi_{i2h}^{n+1}, \nabla\varphi_h) + (H^*, \varphi_h) + \dfrac{S_1}{\epsilon^2}(\phi_{i2h}^{n+1}, \varphi_h), i = 1, 2, \end{cases} \tag{3.72}$$

$$\begin{cases} \dfrac{a}{2M_2\delta t}(\psi_{i1h}^{n+1}, \varpi_h) = -(\nabla\omega_{i1h}^{n+1}, \nabla\varpi_h) + \hat{G}_{i1}, \\ (\omega_{i1h}^{n+1}, \Psi_h) = \lambda_2\gamma(\nabla\psi_{i1h}^{n+1}, \nabla\Psi_h) + \dfrac{S_2}{\eta^2}(\psi_{i1h}^{n+1}, \Psi_h), i = 1, 2, \end{cases} \tag{3.73}$$

$$\begin{cases} \dfrac{a}{2M_2\delta t}(\psi_{i2h}^{n+1}, \varpi_h) = -(\nabla\omega_{i2h}^{n+1}, \nabla\varpi_h) + \hat{G}_{i2}, \\ (\omega_{i2h}^{n+1}, \Psi_h) = \lambda_2\gamma(\nabla\psi_{i2h}^{n+1}, \nabla\Psi_h) + (R^*, \Psi_h) + \dfrac{S_2}{\eta^2}(\psi_{i2h}^{n+1}, \Psi_h), i = 1, 2, \end{cases} \tag{3.74}$$

where

$$\begin{cases} G_{11} = (\dfrac{b\phi_h^n - c\phi_h^{n-1}}{2M_1\delta t}, \Theta_h), G_{21} = \dfrac{1}{M_1}(\mathbf{u}_h^*\phi_h^*, \nabla\Theta_h), G_{12} = G_{22} = 0, \\ \hat{G}_{11} = (\dfrac{b\psi_h^n - c\psi_h^{n-1}}{2M_2\delta t}, \varpi_h), \hat{G}_{21} = \dfrac{1}{M_2}(\mathbf{u}_h^*\psi_h^*, \nabla\varpi_h), \hat{G}_{12} = \hat{G}_{22} = 0. \end{cases} \tag{3.75}$$

It is very easy to solve (3.71)–(3.74) since all equations in these systems are linear and elliptic with constant coefficients. Note that $\phi_{12h}^{n+1}=\phi_{22h}^{n+1}$ and $\psi_{12h}^{n+1}=\psi_{22h}^{n+1}$, thus we only need to solve six elliptic systems here.

Step 2:, we further solve U_1^{n+1} and U_2^{n+1}. We rewrite (3.36) to be the following form:

$$U^{n+1}=\frac{1}{2}\int_\Omega(H^*\phi_h^{n+1}+R^*\psi_h^{n+1})d\boldsymbol{x}+g^n, \tag{3.76}$$

where $g^n=\frac{1}{3}(bU^n-cU^{n-1})-\frac{1}{6}\int_\Omega(H^*(b\phi_h^n-c\phi_h^{n-1})+R^*(b\psi_h^n-c\psi_h^{n-1}))d\boldsymbol{x}$, and replace $(U,\phi_h,\psi_h)^{n+1}$ using (3.65) to get

$$U_1^{n+1}+Q^{n+1}U_2^{n+1}=\frac{1}{2}\int_\Omega(H^*(\phi_{1h}^{n+1}+Q^{n+1}\phi_{2h}^{n+1})+R^*(\psi_{1h}^{n+1}+Q^{n+1}\psi_{2h}^{n+1}))d\boldsymbol{x}+g^n. \tag{3.77}$$

According to Q^{n+1}, we get

$$U_i^{n+1}=\frac{1}{2}\int_\Omega(H^*\phi_{ih}^{n+1}+R^*\psi_{ih}^{n+1})d\boldsymbol{x}+G_U^i, i=1,2, \tag{3.78}$$

where $G_U^1=g^n, G_U^2=0$. We continue to replace $\phi_{ih}^{n+1},\psi_{ih}^{n+1}$ with $i=1,2$ in (3.78) using (3.70) and apply a simple factorization to derive

$$U_i^{n+1}=\frac{\frac{1}{2}\int_\Omega(H^*\phi_{i1h}^{n+1}+R^*\psi_{i1h}^{n+1})d\boldsymbol{x}+G_U^i}{1-\frac{1}{2}\int_\Omega H^*\phi_{i2h}^{n+1}d\boldsymbol{x}-\frac{1}{2}\int_\Omega R^*\psi_{i2h}^{n+1}d\boldsymbol{x}}, i=1,2. \tag{3.79}$$

Thus one can directly solve U_1^{n+1},U_2^{n+1} from (3.79) under of the premise that the denominators are non-zero.

We show the solvability of (3.79) as follows. For the system of $(\phi_{i2h},\mu_{i2h})^{n+1}, i=1,2$ in (3.72), we set $\Theta_h=-\mu_{i2h}^{n+1}$ and $\varphi_h=\frac{a}{2M_1\delta t}\phi_{i2h}^{n+1}$ to deduce

$$-\frac{a}{2M_1\delta t}\int_\Omega H^*\phi_{i2h}^{n+1}d\boldsymbol{x}=\|\nabla\mu_{i2h}^{n+1}\|^2+\frac{\lambda_1 a}{2M_1\delta t}\|\nabla\phi_{i2h}^{n+1}\|^2+\frac{aS_1}{2M_1\epsilon^2\delta t}\|\phi_{i2h}^{n+1}\|^2\geq 0, i=1,2. \tag{3.80}$$

In the similar way, we set $\varpi_h=-\omega_{i2h}^{n+1}$ and $\Psi_h=\frac{a}{2M_2\delta t}\psi_{i2h}^{n+1}$ in (3.74) to deduce

$$-\frac{a}{2M_2\delta t}\int_\Omega R^*\psi_{i2h}^{n+1}d\boldsymbol{x}=\|\nabla\omega_{i2h}^{n+1}\|^2+\frac{\lambda_2\gamma a}{2M_2\delta t}\|\nabla\psi_{i2h}^{n+1}\|^2+\frac{aS_2}{2M_2\eta^2\delta t}\|\psi_{i2h}^{n+1}\|^2\geq 0, i=1,2. \tag{3.81}$$

Hence, the denominators in (3.79) are always non-zero which means the solvability of (3.79) is always valid. After U_1^{n+1},U_2^{n+1} are computed, $\phi_{ih}^{n+1},\mu_{ih}^{n+1},\psi_{ih}^{n+1},\omega_{ih}^{n+1}$ with $i=1,2$ can be updated from (3.70) directly.

Step 3: we solve the velocity field $\tilde{\mathbf{u}}_h^{n+1}$ in (3.37). We formulate $\tilde{\mathbf{u}}_h^{n+1}$ to be the split form as

$$\tilde{\mathbf{u}}_h^{n+1}=\tilde{\mathbf{u}}_{1h}^{n+1}+Q^{n+1}\tilde{\mathbf{u}}_{2h}^{n+1}. \tag{3.82}$$

After replacing the variable $\tilde{\mathbf{u}}_h^{n+1}$ in (3.37) with (3.82), and splitting the obtained equations in terms of Q^{n+1}, we can obtain two sub-systems:

$$\Big(\big(\frac{a}{2\delta t}+\alpha\nu(\hat{\phi}_h^*)\big)\tilde{\mathbf{u}}_{ih}^{n+1},\boldsymbol{v}_h\Big)=(R_{\mathbf{u}}^i,\boldsymbol{v}_h), i=1,2, \tag{3.83}$$

where $R_{\mathbf{u}}^1=-\nabla p_h^n+\frac{b\mathbf{u}_h^n-c\mathbf{u}_h^{n-1}}{2\delta t}, R_{\mathbf{u}}^2=-\phi_h^*\nabla\mu_h^*-\psi_h^*\nabla\omega_h^*$. It is very easy to solve (3.83) since they are just linear algebraic equations. Moreover, since $\nu(\hat{\phi}_h^*)\geq\min(\nu_1,\nu_2)>0$, we have $\frac{a}{2\delta t}+\alpha\nu(\hat{\phi}_h^*)>0$ which shows (3.83) is always solvable.

Step 4: we solve Q^{n+1} in (3.38). By using the linear combination forms for the variables $(\mu_h, \omega_h)^{n+1}$ in (3.65), $\tilde{\mathbf{u}}_h^{n+1}$ in (3.82), we formulate (3.38) into the following form:

$$(\frac{3}{2\delta t} - \eta_2)Q^{n+1} = \frac{1}{2\delta t}(4Q^n - Q^{n-1}) + \eta_1, \tag{3.84}$$

where η_i is given as

$$\eta_i = \int_\Omega \Big(- \phi_h^* \mathbf{u}_h^* \cdot \nabla \mu_{ih}^{n+1} - \psi_h^* \mathbf{u}_h^* \cdot \nabla \omega_{ih}^{n+1} + \phi_h^* \nabla \mu_h^* \cdot \tilde{\mathbf{u}}_{ih}^{n+1} + \psi_h^* \nabla \omega_h^* \cdot \tilde{\mathbf{u}}_{ih}^{n+1} \Big) d\boldsymbol{x}, i = 1, 2. \tag{3.85}$$

It is very easy to solve (3.84) since all terms in η_1 and η_2 are already obtained from Step 1-Step 3 (solvability of (3.84) is given below). Once Q^{n+1} is obtained from (3.84), $\tilde{\mathbf{u}}_h^{n+1}$ is updated from (3.82), and $\phi_h^{n+1}, \mu_h^{n+1}, \psi_h^{n+1}, \omega_h^{n+1}, U^{n+1}$ are updated from (3.65).

We further show the solvability of (3.84), *i.e.*, $\frac{3}{2\delta t} - \eta_2 \neq 0$. Taking $\boldsymbol{v}_h = \tilde{\mathbf{u}}_{2h}^{n+1}$ in the equation (3.83) for $i = 2$, we deduce

$$-\int_\Omega \Big(\phi_h^* \nabla \mu_h^* \cdot \tilde{\mathbf{u}}_{2h}^{n+1} + \psi_h^* \nabla \omega_h^* \cdot \tilde{\mathbf{u}}_{2h}^{n+1} \Big) d\boldsymbol{x} = \frac{a}{2\delta t} \|\tilde{\mathbf{u}}_{2h}^{n+1}\|^2 + \alpha \| \sqrt{\nu(\hat{\phi}_h^*)} \tilde{\mathbf{u}}_{2h}^{n+1} \|^2 \geq 0. \tag{3.86}$$

Taking $\Theta_h = -M_1 \mu_{2h}^{n+1}$, $\varphi_h = \frac{a}{2\delta t} \phi_{2h}^{n+1}$ in (3.67), $\varpi_h = -M_2 \omega_{2h}^{n+1}$, $\Psi_h = \frac{a}{2\delta t} \psi_{2h}^{n+1}$ in (3.69), and combining the four obtained equalities, we get

$$\begin{aligned} &\int_\Omega (\phi_h^* \mathbf{u}_h^* \cdot \nabla \mu_{2h}^{n+1} + \psi_h^* \mathbf{u}_h^* \cdot \nabla \omega_{2h}^{n+1}) d\boldsymbol{x} \\ &\quad = M_1 \|\nabla \mu_{2h}^{n+1}\|^2 + \frac{a\lambda_1}{2\delta t} \|\nabla \phi_{2h}^{n+1}\|^2 + \frac{aS_1}{2\delta t \epsilon^2} \|\phi_{2h}^{n+1}\|^2 \\ &\quad + M_2 \|\nabla \omega_{2h}^{n+1}\|^2 + \frac{a\lambda_2 \gamma}{2\delta t} \|\nabla \psi_{2h}^{n+1}\|^2 + \frac{aS_2}{2\delta t \eta^2} \|\psi_{2h}^{n+1}\|^2 \\ &\quad + \frac{a}{2\delta t} U_2^{n+1} \int_\Omega \left(H^* \phi_{2h}^{n+1} + R^* \psi_{2h}^{n+1} \right) d\boldsymbol{x}. \end{aligned} \tag{3.87}$$

From (3.78) with $i = 2$, we get

$$U_2^{n+1} \int_\Omega (H^* \phi_{2h}^{n+1} + R^* \psi_{2h}^{n+1}) d\boldsymbol{x} = 2(U_2^{n+1})^2 \geq 0, \tag{3.88}$$

which implies

$$\int_\Omega (\phi_h^* \mathbf{u}_h^* \cdot \nabla \mu_{2h}^{n+1} + \psi_h^* \mathbf{u}_h^* \cdot \nabla \omega_{2h}^{n+1}) d\boldsymbol{x} \geq 0. \tag{3.89}$$

The combination of (3.86) and (3.89) gives $-\eta_2 \geq 0$. Thus (3.84) is always solvable.

Step 5: we update $\mathbf{u}_h^{n+1}$ and p_h^{n+1} from (3.39) and (3.40).

From the above-detailed implementation process, it can be seen that the calculation of all unknown variables are completely decoupled. At each time step, the total cost only includes the computations of several elliptic equations. The decoupling of all equations and the characteristic of having only constant coefficients means very efficient practical calculations.

Remark 3.9. For the sake of completeness, here we present the fully-decoupled scheme developed in [22] for solving the Darcy coupled Cahn-Hilliard equation. For simplicity, only the first-order time marching scheme is given here, since the second-order version follows the same line. We only discretize related terms, while other irrelevant terms remain unchanged. The scheme in [22] reads as

$$\phi_t + \nabla \cdot (\mathbf{u}^{n+1}\phi^n) = M\Delta\mu^{n+1}, \tag{3.90}$$

$$\tau\frac{\mathbf{u}^{n+1}-\mathbf{u}^n}{\delta t} + \alpha\nu(\phi)\mathbf{u}^{n+1} + \nabla p^n + \phi^n\nabla\mu^{n+1} = 0. \tag{3.91}$$

Note that the advection $\nabla \cdot (\mathbf{u}\phi)$ and surface tension $\phi\nabla\mu$ are discretized using the traditional explicit-implicit combination method. Due to the special format of the Darcy equations, by using the explicit linear relationship between $\mathbf{u}^{n+1}$ and other items, the decoupling structure of the above scheme can be obtained. More precisely, one can rewrite (3.91) as

$$\mathbf{u}^{n+1} = \frac{1}{\frac{\tau}{\delta t} + \alpha\nu(\phi)}\Big(\frac{\tau}{\delta t}\mathbf{u}^n - \nabla p^n + \phi^n\nabla\mu^{n+1}\Big). \tag{3.92}$$

Then, by replacing $\mathbf{u}^{n+1}$ in the scheme (3.90) using (3.92), the scheme for the Cahn-Hilliard equation is formulated as

$$\phi_t + \nabla \cdot \Big(\frac{1}{\frac{\tau}{\delta t} + \alpha\nu(\phi)}\big(\frac{\tau}{\delta t}\mathbf{u}^n - \nabla p^n + \phi^n\nabla\mu^{n+1}\big)\phi^n\Big) = M\Delta\mu^{n+1}. \tag{3.93}$$

This scheme does achieve a full decoupling structure, *i.e.*, the computation of ϕ^{n+1} is independent of the velocity field $\mathbf{u}^{n+1}$. However, the paid price is that the phase-field equation is then equipped with variable coefficients (*i.e.*, the coefficients of μ^{n+1}) at each time step, which increases the practical computational cost.

Moreover, it is worth noting that if we apply similar techniques to the DCHS model studied here, (3.92) will also include $\psi^n\nabla\omega^{n+1}$. This means the two Cahn-Hilliard equations must be coupled together. Therefore, the decoupling technique given in [22] can not actually obtain the expected full decoupling structure for the DCHS model.

4. NUMERICAL SIMULATION

In this section, we investigate the accuracy, energy stability, and effectiveness of the proposed scheme (3.32)–(3.40), numerically, in which all the numerical simulation are implemented using the FreeFem++ [23].

4.1. Accuracy and stability test

In this example, we perform several convergence and stability tests in 2D of the finite element scheme (3.32)–(3.40), referred to as DSAV for short. We set the computational domain as $\Omega = [0,2]^2$. We use $l = \ell = 2$, that is, $P2$ finite elements for ϕ, ψ, μ, ω, p, and $P1$ for $\mathbf{u}$.

We first verify the convergence order of the scheme DSAV in space and time, where we impose some suitable source terms so that the following solutions satisfy the system (2.4)–(2.7):

$$\begin{cases} \phi(x,y,t) = \cos(2\pi x)\cos(\pi y)\cos t, \psi(x,y,t) = 0.2 + 0.01\cos(4\pi x)\cos(4\pi y)\cos t, \\ \mathbf{u}(x,y,t) = (u(x,y,t), v(x,y,t)) = (\pi\sin(2\pi y)\sin^2(\pi x), -\pi\sin(2\pi x)\sin^2(\pi y)\cos t), \\ p(x,y,t) = \cos(\pi x)\cos(\pi y)\sin t. \end{cases} \tag{4.1}$$

We set the model parameters as

$$\begin{aligned} &\nu_1 = \nu_2 = 1, \alpha = 1e3, \lambda_1 = \lambda_2 = 1e-2, \gamma = 1, \tau = 1, \zeta = 1e-5, \\ &\theta = 0.01, \epsilon = 0.09, \eta = 5e-3, M_1 = M_2 = 1, B = 1e5, S_1 = S_2 = 4. \end{aligned} \tag{4.2}$$

To verify the temporal convergence order, the linear relation between the spatial resolution and temporal resolution is assumed such that the temporal error is dominant. In Figure 1a, the errors measured in L^2 norm

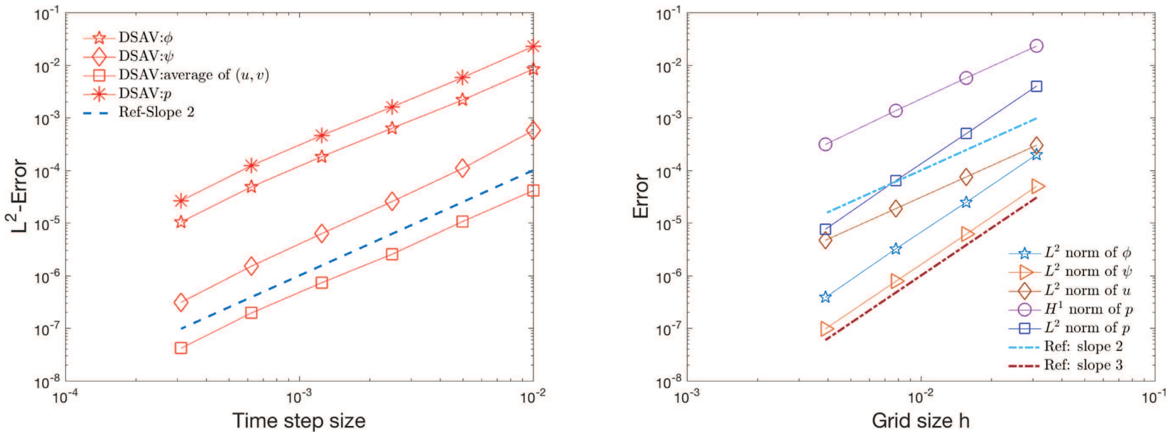

(a) (b)

FIGURE 1. Convergence order tests for (a) temporal and (b) spatial discretization for the example of the presumed exact solutions (4.1).

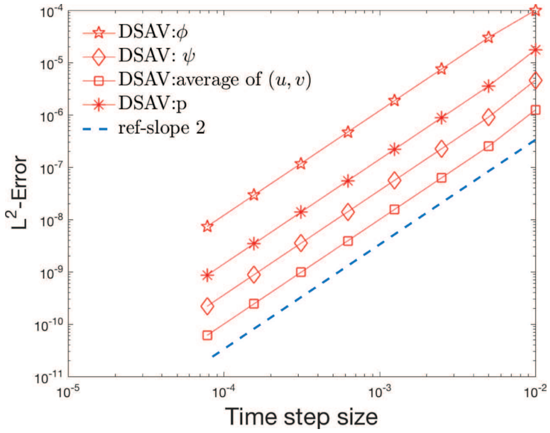

FIGURE 2. Convergence order tests for temporal discretization for the example of the presumed exact solutions (4.1) with low stiffness parameters with low stiffness parameters of $\eta = \epsilon = 1, \theta = 0.001$.

between the numerical solution and the exact solution at $t = 1$ are plotted, where we vary different time step size and the spatial grid size is set as $h = \delta t$. It can be observed that the scheme DSAV presents second-order temporal accuracy for all variables.

To verify the spatial convergence order, in Figure 1b, we plot the errors measured in various norms at $t = 1$ for various mesh size h, in which we choose δt sufficiently small ($\delta t = 1e - 5$) so that the errors are dominated by the spatial discretization error. We can see that the third-order convergence rates are followed by the pressure ϕ, ψ, p in the L^2 norm, while the second-order convergence rates are observed for the $\mathbf{u}$ in the L^2 norm, p in the H^1 norm. These results are in full agreements with the theoretical expectation of accuracy for the adopted finite element space. In Fig. 2, we test the convergence rate for low stiffness parameters $\eta = \epsilon = 1, \theta = 0.001$. It can be seen all variables follow the second-order convergence order.

We further perform the stability test by plotting the time evolution of the total free energy where we set the initial conditions to ϕ to be two circles with different radii, that read as follows (shown in the small inset figure

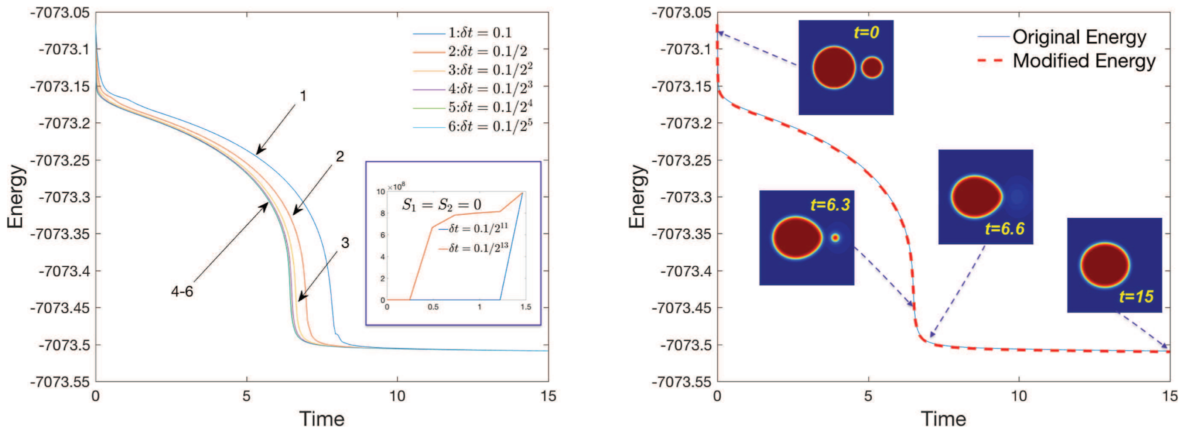

(a) (b)

FIGURE 3. (a) The time evolution of the total free energy (3.48) with different time steps, where small inset subfigure shows that even with very tiny time steps, the energy blows up if $S_1 = S_2 = 0$, and (b) comparisons of the time evolution of the total free energy in the original form (2.15) and in the discrete form (3.48) computed with $\delta t = 0.1/2^3$, where several profiles of ϕ are appended to show the coarsening effects.

in Fig. 3b),

$$\begin{cases} \phi^0(x,y) = 1 + \sum_{i=1}^{2} \tanh(\frac{r_i - \sqrt{(x-x_i)^2 + (y-y_i)^2}}{1.5\epsilon}), \psi^0 = 0.2, \\ \mathbf{u}^0(x,y) = \mathbf{0}, p^0(x,y) = 0, \end{cases} \tag{4.3}$$

where $r_1 = 1.4$, $r_2 = 0.7$, $x_1 = \pi - 0.8$, $x_2 = \pi + 1.7$, $y_1 = y_2 = \pi$. The computational domain is set as $[0, 2\pi]^2$. We still use the model parameters given in (4.2) and grid size $h = \frac{2\pi}{256}$.

In Figure 3a, the evolution curves of the total free energy (3.48) computed by the scheme DSAV are shown, where different time step sizes are used. All energy curves computed show monotonic decays, thereby verifying its unconditional stability. When the time step δt is large (*e.g.*, $\delta t \geq 0.1/2^2$), the obtained energy curves display large deviations from others, which means that the larger the time step, the larger the error. When the time step δt is small (*e.g.*, $\delta t \leq 0.1/2^3$), the obtained energy curves are overlapped, which means that the smaller the time step, the more accurate the computation result. To illustrate the effectiveness of the stabilizations (S_1 and S_2), for comparison, in the small inset figure of Figure 3a, we append the energy curves computed by DSAV but with $S_1 = S_2 = 0$. We find that, with the absence of these two stabilizers, the energy blows up quickly even with very tiny time steps (*e.g.*, $\delta t = 0.1/2^{13}$), which shows these two stabilizers are very effective in improving stability. In Figure 3b, we plot the time evolution of the total free energy in the original form (2.15) and the discrete form (3.48) using the same time step size $\delta t = 0.1/2^3$. Both energy curves overlap very well. We also attach the profiles of ϕ at various times and find that the coarsening effect causes the small circle to gradually absorb into the large circle.

4.2. Saffman-Taylor fingering instability

In this subsection, we simulate the Saffman-Taylor fingering pattern instability problem, which demonstrates the formation and evolution of elaborate patterned structures, as one of the most in-depth benchmark research problems in fluid dynamic systems. It considers the development of interfacial instabilities when a fluid with

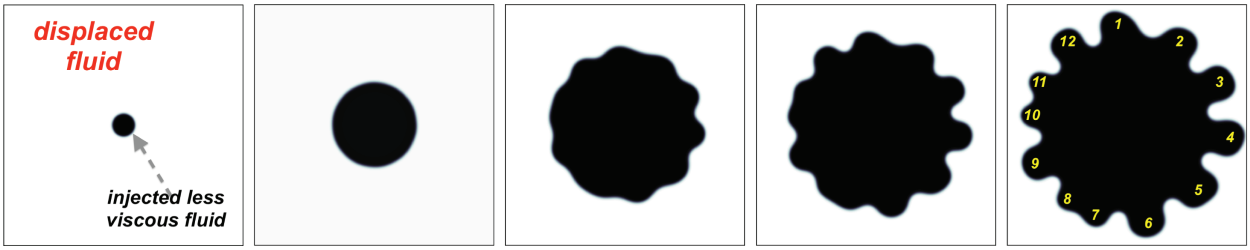

FIGURE 4. Example of radial injection of a less viscous fluid, where the surfactant effect is absent ($\theta = 0$). Snapshots of the phase-field variable ϕ are taken at t = 0, 1, 3, 4, 5.5. In the grayscale images, the dark and blank regions represent the injected fluid with less viscosity and the displaced fluid with higher viscosity, respectively.

low viscosity displaces another fluid of higher viscosity between the narrowly spaced plates of a Hele-Shaw cell. Several widely studied versions of this problem are the so-called continuous injection (radial or uniform) [5, 7, 13, 35], or rotating Hele-Shaw cell [2, 6, 35, 43]. Below we carry out numerical simulations on these three problems respectively. In each case, we compare the number of fingers formed to verify the weakening effects of surface tension by surfactants.

4.2.1. Radial injection of a less viscous fluid

The first numerical example considers a radial injection of low-viscosity fluid to displace high-viscosity fluid. Initially, except for a small circular area in the center of the domain occupied by the low viscosity fluid, the entire domain is filled with a fluid with high viscosity. The two fluids are immiscible, and the low-viscosity fluid intrudes from the center of the domain at a constant injection rate. Physical and numerical experiments show that as the size of the fluid interface increases outward, fingers are formed, spread out and move in the direction of separation from each other, and finally get very complex branching patterns, see [1, 3, 7, 13, 17, 29, 35, 37, 43].

We implement numerical simulations in 2D with the computational domain $\Omega = [0, 2\pi]^2$. To represent the injection flow, we adopt the Gaussian method designed in [43] where a potential radial velocity $\mathbf{u}_p$ is imposed in the momentum equation and the Cahn-Hilliard equation for ϕ. Namely, the two corresponding equations are modified as

$$\phi_t + \nabla \cdot (\mathbf{u}\phi) + (\mathbf{u}_p \cdot \nabla)\phi = M_1 \Delta \mu, \tag{4.4}$$

$$\tau \mathbf{u}_t + \alpha\nu(\phi)(\mathbf{u} + \mathbf{u}_p) + \nabla p + \phi\nabla\mu + \psi\nabla\omega = 0, \tag{4.5}$$

where $\mathbf{u}_p = -C(1 - e^{-4r^2/R_0^2})\tilde{\mathbf{r}}, r = \sqrt{(x - x_0)^2 + (y - y_0)^2}, \tilde{\mathbf{r}}(x, y) = (\frac{x - x_0}{r + \varepsilon}, \frac{y - y_0}{r + \varepsilon})$, C is the injection strength, R_0 is the radius of the circular injection region, ε is a small quantity such that $r + \varepsilon \neq 0$.

We set the initial conditions as follows:

$$\phi^0 = \tanh(\frac{\tilde{r} - \sqrt{(x - x_0)^2 - (y - y_0)^2}}{\epsilon}), \psi^0 = 0.2, \mathbf{u}^0 = (0, 0), p^0 = 0, \tag{4.6}$$

where $\tilde{r} = r_0 + 0.01\text{rand}(\boldsymbol{x})$ and $\text{rand}(\boldsymbol{x})$ is the random number in $[-1, 1]$. We set model parameters as

$$\begin{aligned}
&x_0 = y_0 = \pi, r_0 = R_0 = 0.3, C = 0.65, \tau = 1, \alpha = 28000, \zeta = 1e - 5,\\
&\epsilon = 0.03, \eta = 1e - 3, \lambda_1 = \lambda_2 = 1e - 3, B = 1e5, S_1 = S_2 = 4,\\
&M_1 = M_2 = 1e - 2, \varepsilon = 1e - 3, \nu_1 = 1, \nu_2 = 0.1, h = 2\pi/512, \delta t = 1e - 3,
\end{aligned} \tag{4.7}$$

where ν_1 is the (high) viscosity of the displaced fluid, ν_2 is the (low) viscosity of the injected fluid. The profile of the initial condition ϕ^0 is shown in Figure 4a. We change the coupling parameter θ to investigate the effect of the surfactant on finger formation.

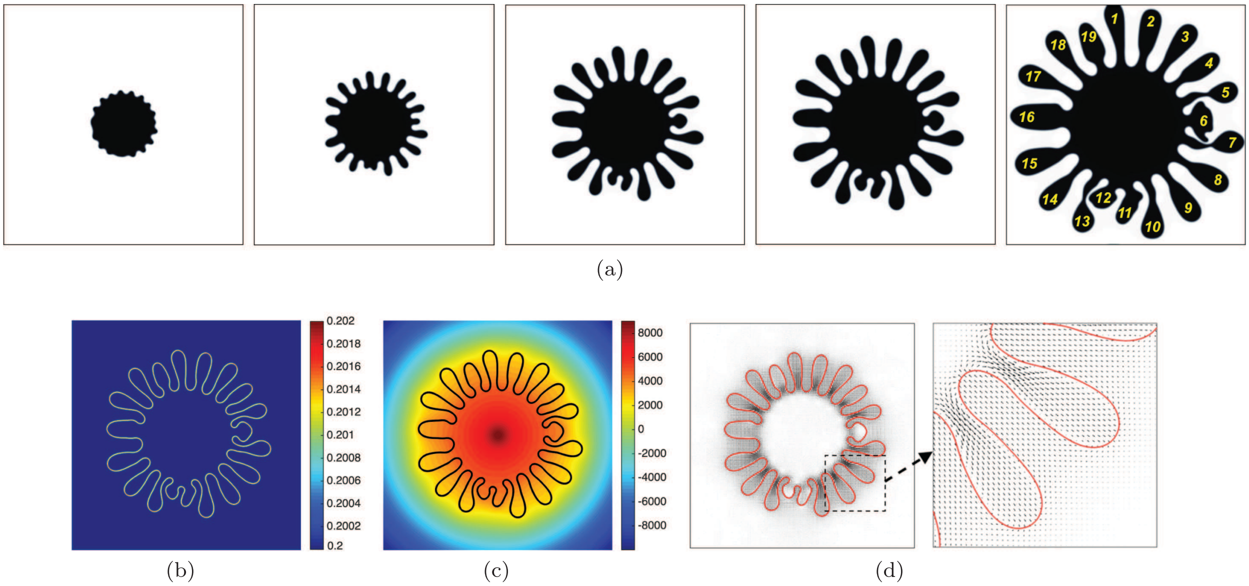

(a)

(b) (c) (d)

FIGURE 5. Example of radial injection of a less viscous fluid with the surfactant effect ($\theta = 0.004$), where (a) snapshots of the phase-field variable ϕ (grayscale image) are captured at $t = 0.5,\ 1,\ 2,\ 2.5,\ 4$; (b) the profile of ψ at $t = 2.5$; (c) the profile of p at $t = 2.5$ (the contour line $\{\phi = 0\}$ appended); and (d) the velocity field $\mathbf{u}$ at $t = 2.5$ (the contour line $\{\phi = 0\}$ appended).

We first set the coupling parameter $\theta = 0$ to study the way the fingers are formed without surfactants. In Figure 4, snapshots of the phase-field variable ϕ at different times are drawn, in which a grayscale image is used to obtain a clearer view. It can be seen that when the fluid with lower viscosity is continuously injected into the domain, and the size of the droplet increases to a certain size, some short and thick fingers are formed (12 fingers marked in the last subfigure of Fig. 4).

We further apply the surfactant effect by setting $\theta = 0.004$ and show snapshots of ϕ at different times in Figure 5a. Unlike the case without surfactants, the number of finger-like patterns finally obtained not only far exceeds (19 fingers, shown in the last subfigure of Fig. 4), but the formed finger shows more slender and longer structure, which indicates that the applied surfactant effectively weakens the surface tension. In Figure 5b, the profile of ψ at $t = 2.5$ is drawn, where one can see that the surfactant concentration is high around the fluid interface due to the coupling term between ϕ and ψ. In Figure 5c and d, we plot the pressure p and the velocity field at $t = 2.5$ where the contour line $\{\phi = 0\}$ is appended. It can be seen that the velocity field presents a radial pattern in the vicinity of each finger.

In Figure 6, by using various coupling parameter θ, we show the fingering pattern at the same time instance $t = 3.5$, where the larger θ (stronger surfactant action) results in a slender finger structure and an increase in the number of fingers, which means that the surfactant has a stronger weakening effect on surface tension. For example, when $\theta = 0.001$, 11 fingers are formed; when $\theta = 0.002$, 14 fingers are formed; when $\theta = 0.003$, 16 fingers are formed; and when $\theta = 0.004$, 19 fingers are formed. These numerical simulations are qualitatively consistent with the physical experiments/numerical simulations in [1,3,5,7,17,29,43].

4.2.2. Uniform injection of a less viscous fluid

The second example is the injection problem similar to the previous example. We still inject low-viscosity fluid, but the injection location is changed to the bottom of the computational domain. The initial conditions are

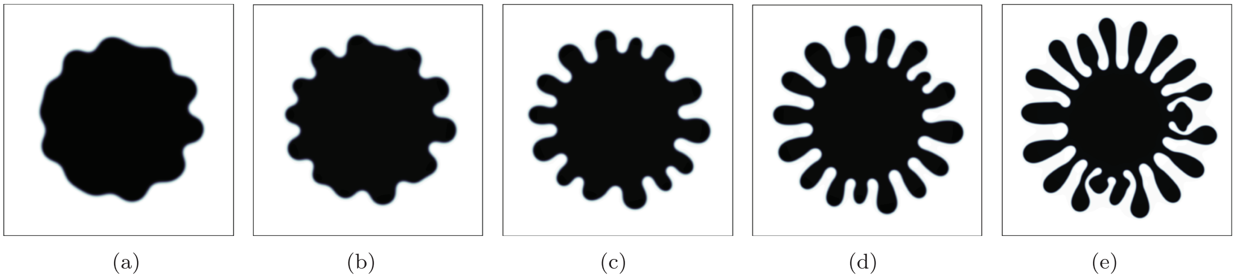
(a) (b) (c) (d) (e)

FIGURE 6. Comparisons of formed fingering patterns of the radial injetion example where different surfactant effects are applied by setting the coupling parameter θ as θ is (a) $\theta = 0$ (no surfactant case); (b) $\theta = 0.001$; (c) $\theta = 0.002$; (d) $\theta = 0.003$; (e) $\theta = 0.004$. In all subfigures, the profiles of ϕ at $t = 3.5$ are plotted in the grayscale image.

set to two fluids with a horizontally layered interface, where the high-viscosity fluid I (blank) is above the low-viscosity fluid II (black), shown in Figure 7a. The Gaussian method designed in [43] using the external potential velocity and the system (4.4)–(4.5) are still used, where $\mathbf{u}_p = (0, v_p)$ for 2D with $v_p = C(\frac{1}{2} - \frac{1}{2}\tanh(y - R_0/0.01))$, and $\mathbf{u}_p = (0, 0, w_p)$ for 3D with $w_p = C(\frac{1}{2} - \frac{1}{2}\tanh(z - R_0/0.01))$, C is the injection strength, R_0 is the width of the injection layer.

We first simulate the 2D example where the computational domain is $(x, y) \in \Omega = [0, 2\pi]^2$. The initial conditions are set as

$$\phi^0 = -\tanh(\frac{y - \tilde{r}}{\epsilon}), \psi^0 = 0.2, \mathbf{u}^0 = (0, 0), p^0 = 0, \tag{4.8}$$

where $\tilde{r} = 0.2 + 0.01\text{rand}(\boldsymbol{x})$. We set the model parameters as

$$\begin{aligned} &R_0 = 0.2, C = 1, \tau = 1, \alpha = 1000, \zeta = 1e-5, \epsilon = 0.09, \\ &\eta = 1e-3, \lambda_1 = \lambda_2 = 1e-2, B = 1e5, S_1 = S_2 = 4, \\ &M_1 = M_2 = 1e-2, \nu_1 = 1, \nu_2 = 0.1, h = 2\pi/512, \delta t = 1e-3. \end{aligned} \tag{4.9}$$

First, by setting $\theta = 0$ to remove the surfactant effect, in Figure 7, we plot the profiles of ϕ at various times using the grayscale image. When the interfacial layer rises to a certain height, fingering structures (8 fingers) appear, and they finally touch the upper wall (at $t = 4.5$). Then, we apply the surfactant effect by setting $\theta = 0.004$. In Figure 8a, snapshots of the phase-field variable ϕ at different times are drawn, in which we can see the significant influence of the surfactant on the surface tension, that is, more slender fingers (15 fingers) are produced over time. The surfactant concentration ψ, pressure p and velocity field $\mathbf{u}$ at $t = 2$ are plotted in In Figure 8b, c, d, respectively.

We further simulate the 3D numerical example with the computational domain of $(x, y, z) \in \Omega = [0, 1.25\pi] \times [0, 0.25\pi] \times [0, 1.25\pi]$. The initial conditions of the layered fluids as

$$\phi^0 = -\tanh(\frac{z - \tilde{r}}{\epsilon}), \psi^0 = 0.2, \mathbf{u}^0 = (0, 0, 0), p^0 = 0, \tag{4.10}$$

where $\tilde{r} = 0.2 + 0.01\text{rand}(\boldsymbol{x})$. We set $h = \frac{1.25\pi}{300}$ and $\delta t = 0.001$. All other model parameters are given in (4.7) with the application of surfactant effect $\theta = 0.004$. The isosurfaces $\{\phi = 0\}$ at the different times are shown in Figure 9, where we can see that a large number of 3D fingers grow vertically upwards over time. These fingering patterns in 2D and 3D are well consistent with the numerical/physical experiments in [15, 32, 33, 35–37, 46], qualitatively.

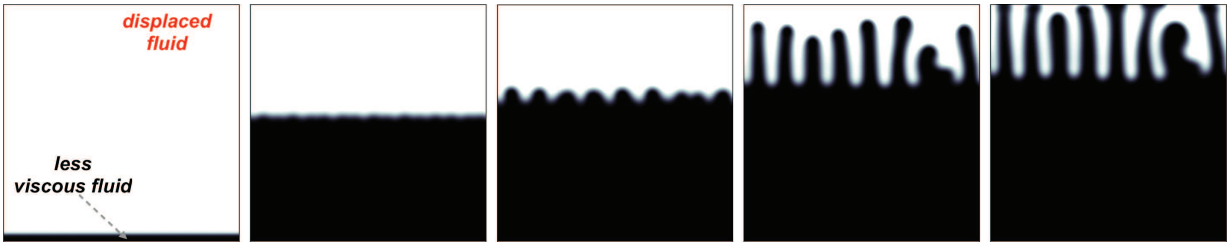

FIGURE 7. Example of uniform injection of a less viscous fluid from the bottom, where surfactant effect is absent ($\theta = 0$). Snapshots of the phase-field variable ϕ are taken at $t = 0$, 2.5, 3, 4, 4.5. In the grayscale images, the dark and blank regions represent the injected fluid with less viscosity and the displaced fluid with higher viscosity, respectively.

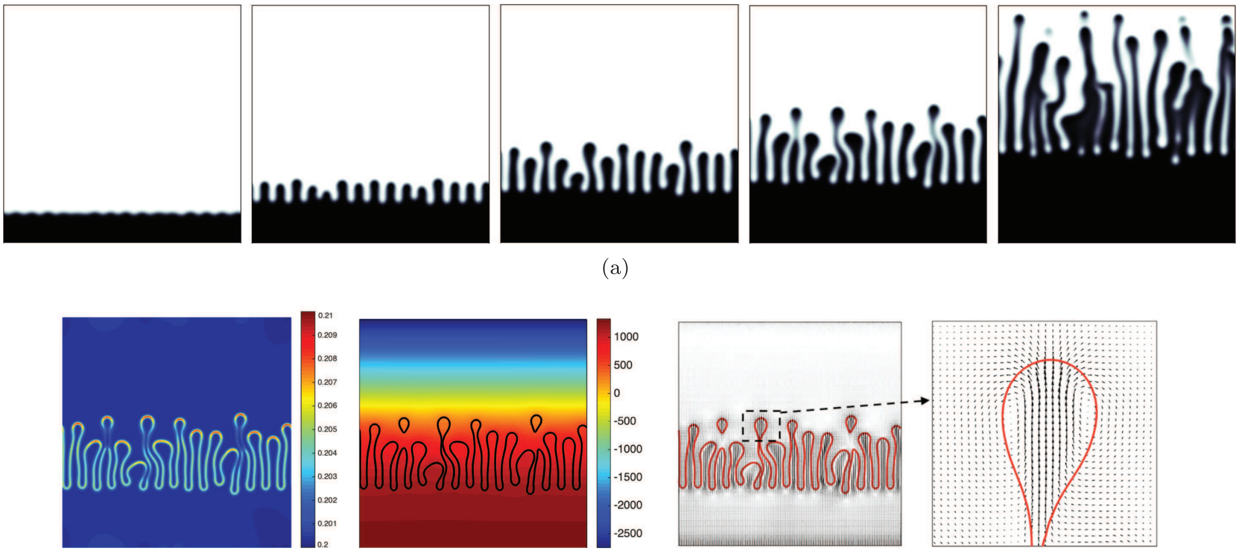

(a)

(b) (c) (d)

FIGURE 8. Example of uniform injection of a less viscous fluid from the bottom with the surfactant effect ($\theta = 0.004$), where (a) snapshots of the phase-field variable ϕ (grayscale image) are taken at $t = 0.5$, 1, 1.5, 2, and 3.5; (b) the profile of ψ at $t = 2$; (c) the profile of p at $t = 2$; and (d) the velocity field $\mathbf{u}$ at $t = 2$.

4.2.3. Rotating Hele-Shaw cell

Rotating the Hele-Shaw cell is another commonly-used method for obtaining fingering patterns, which will be implemented in this example. The rotation state can be achieved by applying an external rotation force in the Darcy equations. More precisely, we replace the momentum equation (2.8) by the following form (see [2, 10]):

$$\tau \mathbf{u}_t + \alpha\nu(\phi)\mathbf{u} + \nabla p + \phi\nabla\mu + \psi\nabla\omega = \boldsymbol{f}_{rot}, \tag{4.11}$$

where $\boldsymbol{f}_{\text{rot}} = \Upsilon_g \frac{(1+\phi)}{2}(\Upsilon_\omega^2 \boldsymbol{r} + 2\Upsilon_\omega(e_z \times \mathbf{u}))$ is the applied rotating force, $e_z = (0,0,1)$, $\boldsymbol{r} = \boldsymbol{x} - \boldsymbol{x}_0$, and Υ_g, Υ_w are constants given in (4.12).

We set $\Omega = [0, 2\pi]^2$ and implement 2D simulations first. The initial conditions of are still from (4.6) with $\tilde{r} = 1.3 + 0.01\text{rand}(\boldsymbol{x})$, and the profile of ϕ^0 is plotted in Figure 10a using the grayscale image. The model

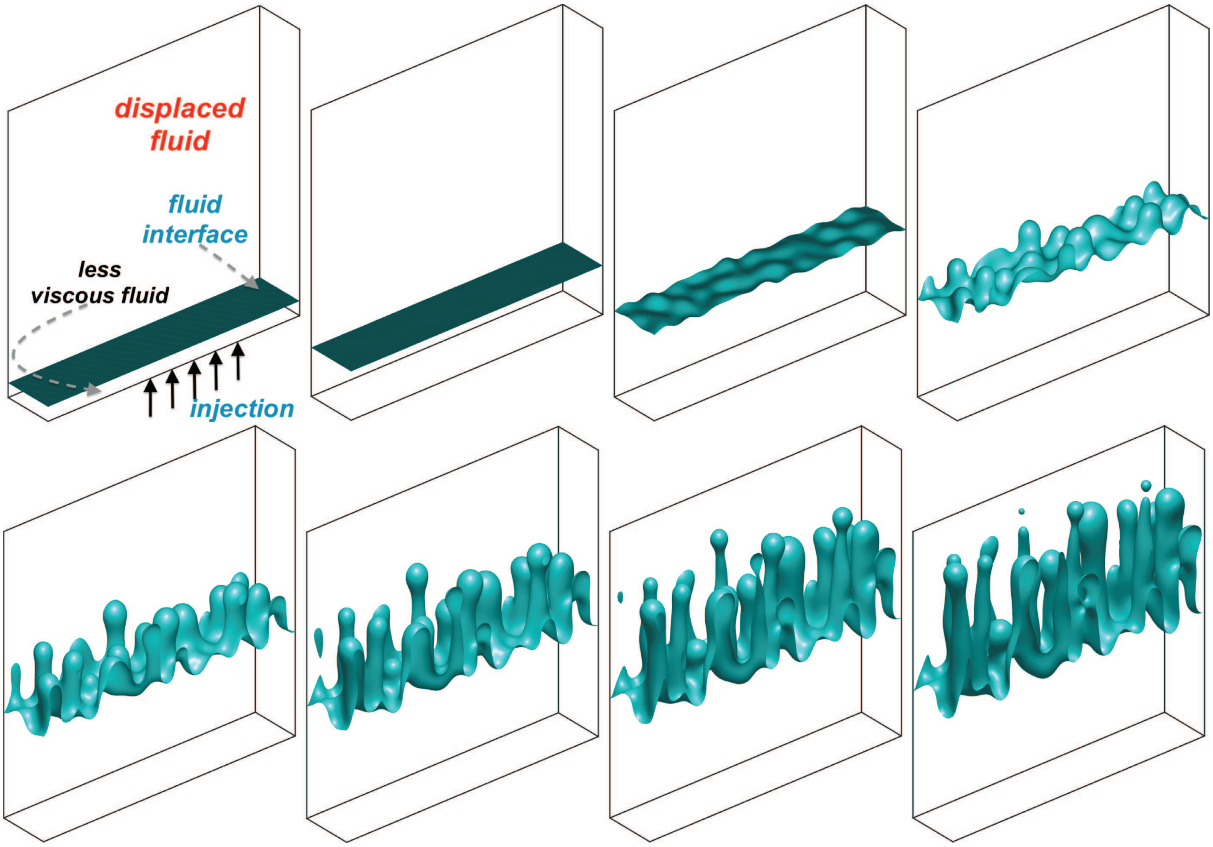

FIGURE 9. Example of 3D uniform injection of a less viscous fluid from the bottom with the surfactant effect ($\theta = 0.004$). Snapshots of the isosurface $\{\phi = 0\}$ are taken at $t = 0$, 0.4, 0.8, 1, 1.2, 1.4, 1.6, and 1.8 from left to right and from top to bottom.

parameters are set as

$$\begin{aligned}&\Upsilon_g = 5, \Upsilon_w = 5, \boldsymbol{x}_0 = (\pi,\pi), \tau = 1, \alpha = 1000, \zeta = 1e-5,\\ &\epsilon = 0.03, \eta = 1e-3, \lambda_1 = \lambda_2 = 1e-3, B = 1e5, S_1 = S_2 = 4,\\ &M_1 = M_2 = 1e-2, \nu_1 = 1, \nu_2 = 0.1, h = 2\pi/512, \delta t = 1e-3.\end{aligned} \tag{4.12}$$

Similar to the previous injection example, we still perform the simulation without the influence of surfactant first, and then study the pattern differences caused by surfactants. In Figure 10, for the case of no surfactant ($\theta = 0$), snapshots of the phase-field variable ϕ at different times are drawn using the grayscale image. We observe that over time, many slender fingers are formed, some of which break into satellite droplets or more branched fingers. We further apply the surfactant effect by setting $\theta = 0.004$. In Figure 11, the phase-field variable ϕ and the concentration variable ψ are plotted at different times. It can be seen that the number of fingers obtained far exceeds the number of fingers without surfactant, which again illustrates the effect of surfactants on weakening the surface tension. In Figure 12, by using various coupling parameter θ, we show the fingering pattern at the same time instance $t = 3$, where the larger θ causes a larger number of fingers with more elongated and slender shapes.

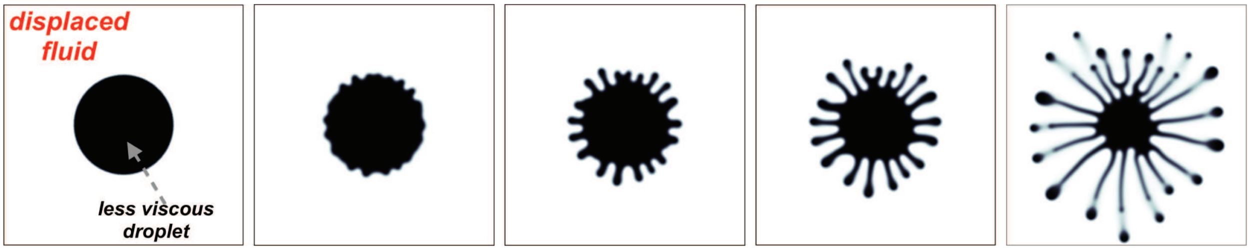

Figure 10. Example of 2D rotating Hele-Shaw cell where the surfactant effect is absent ($\theta = 0$). Snapshots of the phase-field variable ϕ are taken at $t = 0, 1, 1.5, 2, 3.2$ (grayscale image).

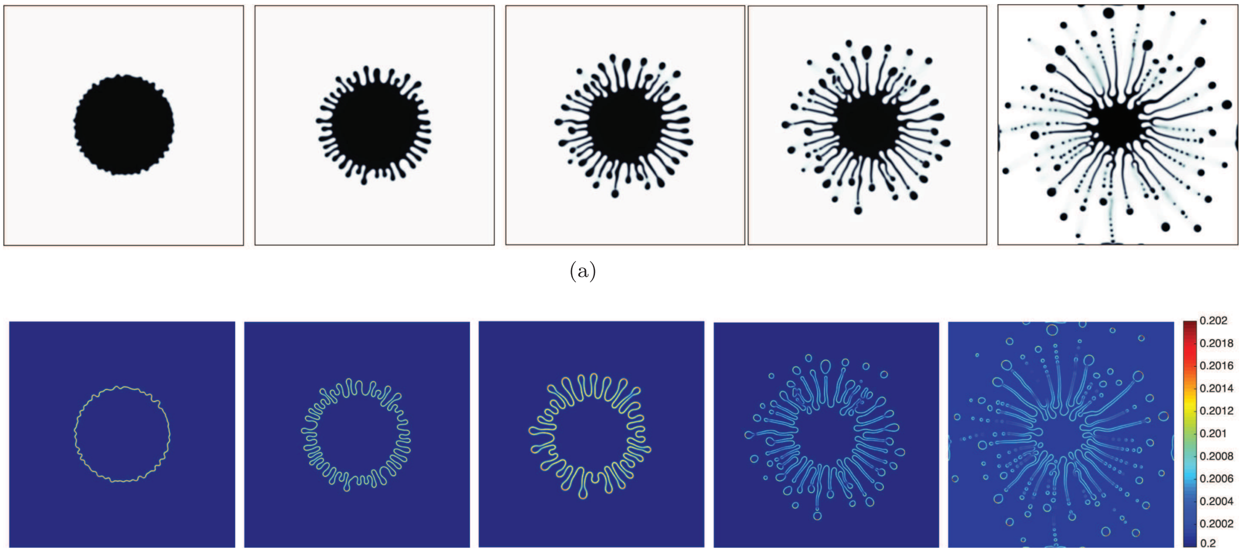

(a)

(b)

Figure 11. Example of 2D rotating Hele-Shaw cell with the surfactant effect ($\theta = 0.004$), where (a) snapshots of the phase-field variable ϕ (grayscale image) and (b) the profile of ψ (color image) are taken at different times.

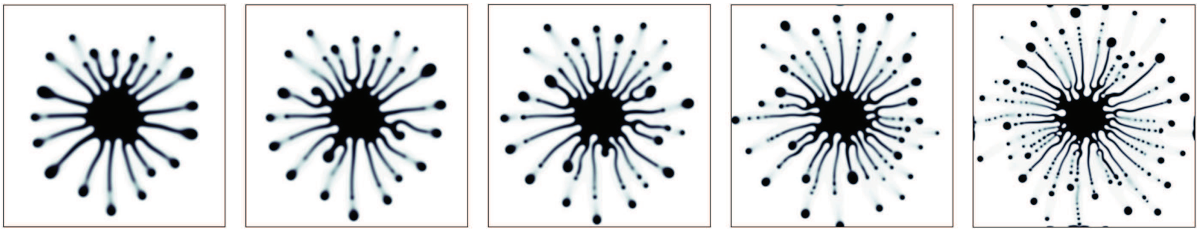

(a) (b) (c) (d) (e)

Figure 12. Comparisons of formed fingers of the 2D rotating Hele-Shaw cell example where different surfactant effects are applied with (a) $\theta = 0$ (no surfactant case); (b) $\theta = 0.001$; (c) $\theta = 0.002$; (d) $\theta = 0.003$; (e) $\theta = 0.004$. In all subfigures, the profiles of ϕ at $t = 3$ are plotted in the grayscale image.

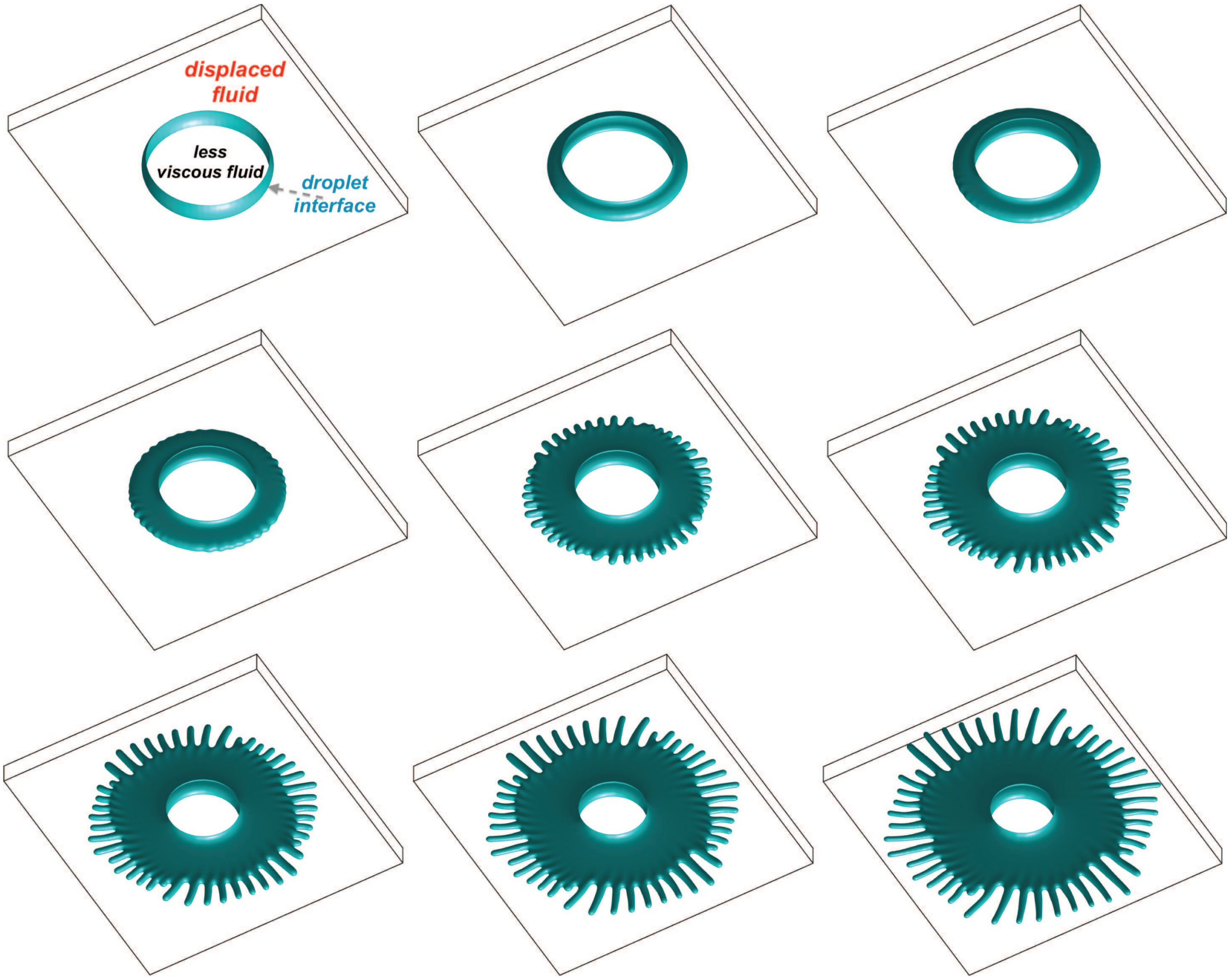

FIGURE 13. Example of the 3D rotating Hele-Shaw cell with the surfactant effect ($\theta = 0.004$) where the isosurfaces $\{\phi = 0\}$ at $t = 0$, 0.4, 0.6, 0.8, 1.2, 1.4, 1.6, 1.8, and 2 are plotted from left to right and from top to bottom.

We continue to perform a simulation in 3D and set the computed domain as $\Omega = [0, 2\pi] \times [0, 2\pi] \times [0, \frac{4\pi}{25}]$. The initial conditions read as (shown in the first subfigure of Fig. 13):

$$\phi^0 = \tanh\left(\frac{\tilde{r} - \sqrt{(x - x_0)^2 - (y - y_0)^2 + (z - z_0)^2}}{\epsilon}\right), \psi^0 = 0.2, \mathbf{u}^0 = (0, 0, 0), p^0 = 0, \tag{4.13}$$

where $x_0 = y_0 = \pi, z_0 = \frac{2\pi}{25}, \tilde{r} = 1 + 0.01\mathrm{rand}(\boldsymbol{x})$. We set the grid size $h = \frac{4\pi}{800}$ and the time step size $\delta t = 0.001$, and all other order parameters are still from (4.12). In Figure 13, the isosurfaces of $\{\phi = 0\}$ at different times are plotted. We observe that that plenty of 3D fingers are formed over time, which are consistent with the 2D simulations qualitatively. Similar dynamics were also observed experimentally/numerically in [2, 3, 6, 10].

5. Concluding remarks

We design a decoupled fully-discrete finite element scheme to solve the highly complex nonlinear Darcy flow-coupled Cahn-Hilliard phase-field model of binary surfactants. The scheme is constructed based on a combination of a variety of effective numerical methods, including the finite element method, projection method, quadratization method, as well as a new decoupling technique by designing a special type of ODE. While maintaining the second-order time accuracy and linearity, it is natural to obtain unconditional energy stability and practically realized decoupling structure. The detailed actual realization, solvability and stability are given rigorously. By simulating plenty of 2D and 3D numerical examples, including the fingering instability caused by radial/uniform injection and rotating Hele-Shaw cell, we numerically prove the effectiveness of the developed scheme. To the best of the author's knowledge, the developed scheme is the first "ideal" type fully-discrete scheme for the Darcy flow coupling binary surfactant phase-field model.

Acknowledgements. This author's research is partially supported by the U.S. National Science Foundation under grant number DMS-2012490.

References

[1] S. Ahmadikhamsi, F. Golfier, C. Oltean, E. Lefèvre and S.A. Bahrani, Impact of surfactant addition on non-newtonian fluid behavior during viscous fingering in Hele-Shaw cell. *Phys. Fluids* **32** (2020) 012103.

[2] E. Álvarez-Lacalle, J. Ortín and J. Casademunt, Low viscosity contrast fingering in a rotating Hele-Shaw cell. *Phys. Fluids* **16** (2004) 908–924.

[3] E. Álvarez-Lacalle, J. Ortín and J. Casademunt, Relevance of dynamic wetting in viscous fingering patterns. *Phys. Rev. E* **74** (2006) 025302.

[4] J. Bear, Dynamics of fluids in porous media, Courier Dover Publications, New York (1988).

[5] I. Bischofberger, R. Ramachandran and S.R. Nagel, An island of stability in a sea of fingers: emergent global features of the viscous-flow instability. *Soft Matter* **11** (2015) 7428–7432.

[6] Ll. Carrillo, F.X. Magdaleno, J. Casademunt and J. Ortín, Experiments in a rotating Hele-Shaw cell. *Phys. Rev. E* **54** (1996) 6260–6267.

[7] J.-D. Chen, Growth of radial viscous fingers in a Hele-Shaw cell. *J. Fluid Mech.* **201** (1989) 223–242.

[8] C. Chen and X. Yang, Efficient Numerical Scheme for a dendritic Solidification Phase Field model with melt convection. *J. Comput. Phys.* **388** (2019) 41–62.

[9] C. Chen and X. Yang, Fast, provably unconditionally energy stable, and second-order accurate algorithms for the anisotropic Cahn-Hilliard Model. *Comput. Meth. Appl. Mech. Eng.* **351** (2019) 35–59.

[10] C.-Y. Chen, Y.-S. Huang and J.A. Miranda, Diffuse-interface approach to rotating Hele-Shaw flows. *Phys. Rev. E* **84** (2011) 046302.

[11] K. Cheng, C. Wang and S.M. Wise, An Energy Stable BDF2 Fourier Pseudo-Spectral Numerical Scheme for the Square Phase Field Crystal Equation. *Commun. Comput. Phys.* **26** (2019) 1335–1364.

[12] M. Chinaud, V. Voulgaropoulos and P. Angeli, Surfactant effects on the coalescence of a drop in a Hele-Shaw cell. *Phys. Rev. E.* **94** (2016) 033101.

[13] J.Y.Y. Chui, P. de Anna and R. Juanes, Interface evolution during radial miscible viscous fingering. *Phys. Rev. E* **92** (2015) 041003.

[14] L. Dede, H. Garcke and K.F. Lam, A hele–shaw–cahn–hilliard model for incompressible two-phase flows with different densities. *J. Math. Fluid Mech.* **20** (2018) 531–567.

[15] C. Derec, P. Boltenhagen, S. Neveu and J.C. Bacri, Magnetic instability between miscible fluids in a Hele-Shaw cell. *Magnetohydrodynamics* **44** (2008) 135–142.

[16] K. Erik Teigen, P. Song, J. Lowengrub and A. Voigt, A diffuse-interface method for two-phase flows with soluble surfactants. *J. Comput. Phys.* **230** (2011) 375–393.

[17] R. Farajzadeh, A.A. Eftekhari, H. Hajibeygi, S. Kahrobaei, J.M. van der Meer, S. Vincent-Bonnieu and W.R. Rossen, Simulation of instabilities and fingering in surfactant alternating gas (sag) foam enhanced oil recovery. *J. Nat. Gas Sci. Eng.* **34** (2016) 1191–1204.

[18] I. Fonseca, M. Morini and V. Slastikov, Surfactants in foam stability: A phase-field approach. *Arch. Ration. Mech. Anal.* **183** (2007) 411–456.

[19] G. Gompper and M. Schick, Self-assembling amphiphilic systems, in phase trasitions and critical phenomena, edited by C. Domb and J. Lebowitz. Academic Press, London, 16 (1994).

[20] S. Gu, H. Zhang and Z. Zhang, An energy-stable finite-difference scheme for the binary fluid-surfactant system. *J. Comput. Phys.* **367** (2014) 3–11.

[21] D. Han and X. Wang, Decoupled energy-law preserving numerical schemes for the cahn–hilliard–darcy system. *Numer. Methods Partial Differ. Equ.* **32** (2016) 936–954.

[22] D. Han and X. Wang, A Second Order in Time, Decoupled, Unconditionally Stable Numerical Scheme for the Cahn–Hilliard–Darcy System. *J. Sci. Comput.* **14** (2018) 1210–1233.

[23] F. Hecht, New development in freefem++. *J. Numer. Math.* **20** (2012) 251–265.

[24] Y.-S. Huang and C.-Y. Chen, A numerical study on radial Hele-Shaw flow: Influence of fluid miscibility and injection scheme. *Comput. Mech.* **55** (2015) 407.

[25] S. Komura and H. Kodama, Two-order-parameter model for an oil-water-surfactant system. *Phys. Rev. E.* **55** (1997) 1722–1727.

[26] M. Laradji, H. Guo, M. Grant and M.J. Zuckermann, The effect of surfactants on the dynamics of phase separation. *J. Phy. Condens. Matter* **4** (1992) 6715.

[27] M. Laradji, O.G. Mouristen, S. Toxvaerd and M.J. Zuckermann, Molecular dynamics simulatiens af phase separation in the presence ef surfactants. *Phys. Rev. E.* **50** (1994) 1722–1727.

[28] H. Liu and Y. Zhang, Phase-field modeling droplet dynamics with soluble surfactants. *J. Comput. Phys.* **229** (2010) 9166–9187.

[29] S. Mollaei and A.H. Darooneh, Spreading, fingering instability and shrinking of a hydrosoluble surfactant on water. *Exp. Therm. Fluid Sci.* **86** (2017) 98–101.

[30] D.A. Nield and A. Bejan, Convection in porous media, Springer-Verlag, New York, 2nd ed. (1999).

[31] K. Okumura, Viscous dynamics of drops and bubbles in Hele-Shaw cells; Drainage, drag fraction, coalescence, and bursting. *Adv. Colloid Inter. Sci.* **225** (2018) 64–75.

[32] S. Pramanik and M. Mishra, Effect of Péclet number on miscible rectilinear displacement in a Hele-Shaw cell. *Phys. Rev. E* **91** (2015) 033006.

[33] S. Pramanik, T.K. Hota and M. Mishra, Influence of viscosity contrast on buoyantly unstable miscible fluids in porous media. *J. Fluid Mech.* **780** (2015) 388–406.

[34] J.-R. Roan and E.I. Shakhnovich, Phase separation of a binary fluid containing surfactants in a Hele-Shaw cell. *Phys. Rev. E* **59** (1999) 2109.

[35] P.G. Saffman and G. Taylor, The penetration of a fluid into a porous medium or Hele-Shaw cell containing a more viscous liquid. *Proc. R. Soc. Lond. A* **245** (1958) 312–329.

[36] P. Satyajit and M. Manoranjan, Nonlinear simulations of miscible viscous fingering with gradient stresses in porous media. *Chem. Eng. Sci.* **122** (2015) 523–532.

[37] V. Sharma, S. Nand, S. Pramanik, C.-Y. Chen and M. Mishra, Control of radial miscible viscous fingering. *J. Fluid Mech.* **884** (2020) A16.

[38] J. Shen and X. Yang, Numerical Approximations of Allen-Cahn and Cahn-Hilliard Equations. *Disc. Contin. Dyn. Sys. A* **28** (2010) 1669–1691.

[39] J. Shen and X. Yang, The IEQ and SAV approaches and their extensions for a class of highly nonlinear gradient flow systems. *Contemp. Math.* **754** (2020) 217–245.

[40] M. Sun, X. Feng and K. Wang, Numerical simulation of binary fluid–surfactant phase field model coupled with geometric curvature on the curved surface. *Comput. Methods Appl. Mech. Eng.* **367** (2020) 113123.

[41] C.H. Teng, I.L.Chern and M.C. Lai, Simulating binary fluid-surfactant dynamics by a phase field model. *Dis. Contin. Dyn. Syst.-B* **17** (2010) 1289–1307.

[42] T. Teramoto and F. Yonezawa, Droplet growth dynamics in a water-oil-surfactant system. *J. Colloid Inter. Sci.* **235** (2001) 329–333.

[43] R. Tsuzuki, Q. Li, Y. Nagatsu and C.-Y. Chen, Numerical study of immiscible viscous fingering in chemically reactive Hele-Shaw flows: Production of surfactants. *Phys. Rev. Fluids* **4** (2019) 104003.

[44] R.G.M. van der Sman and S. van der Graaf, Diffuse interface model of surfactant adsorption onto flat and droplet interfaces. *Rheol. Acta* **46** (2006) 3–11.

[45] R.G.M. van der Sman and M.B.J. Meinders, Analysis of improved lattice boltzmann phase field method for soluble surfactants. *Comput. Phys. Comm.* **199** (2016) 12–21.

[46] R.A. Wooding, Growth of fingers at an unstable diffusing interface in a porous medium or Hele-Shaw cell. *J. Fluid Mech.* **39** (1969) 477–95.

[47] X. Yang, A new efficient Fully-decoupled and Second-order time-accurate scheme for Cahn-Hilliard phase-field model of three-phase incompressible flow. *Comput. Methods Appl. Mech. Eng.* **376** (2021) 13589.

[48] X. Yang, A novel fully-decoupled scheme with second-order time accuracy and unconditional energy stability for the Navier-Stokes equations coupled with mass-conserved Allen-Cahn phase-field model of two-phase incompressible flow. *Int. J. Numer. Methods Eng.* **122** (2021) 1283–1306.

[49] X. Yang, A novel fully-decoupled, second-order and energy stable numerical scheme of the conserved Allen-Cahn type flow-coupled binary surfactant model. *Comput. Methods Appl. Mech. Eng.* **373** (2021) 113502.

[50] X. Yang, A novel fully-decoupled, second-order time-accurate, unconditionally energy stable scheme for a flow-coupled volume-conserved phase-field elastic bending energy model. *J. Comput. Phys.* **432** (2021) 110015.

[51] X. Yang, Efficient and Energy Stable scheme for the hydrodynamically coupled three components Cahn-Hilliard phase-field model using the stabilized-Invariant Energy Quadratization (S-IEQ) Approach. *J. Comput. Phys.* **438** (2021) 110342.

[52] X. Yang, On a novel fully-decoupled, second-order accurate energy stable numerical scheme for a binary fluid-surfactant phase-field model. *SIAM J. Sci. Comput.* **43** (2021) B479–B507.

[53] X. Yang and L. Ju, Linear and unconditionally energy stable schemes for the binary fluid-surfactant phase field model. *Comput. Meth. Appl. Mech. Eng.* **318** (2017) 1005–1029.

[54] X. Yang and H. Yu, Efficient Second Order Unconditionally Stable Schemes for a Phase Field Moving Contact Line Model Using an Invariant Energy Quadratization Approach. *SIAM J. Sci. Comput.* **40** (2018) B889–B914.

[55] J. Zhang and X. Yang, Unconditionally energy stable large time stepping method for the L2-gradient flow based ternary phase-field model with precise nonlocal volume conservation. *Comput. Methods Appl. Mech. Eng.* **361** (2020) 112743.

[56] J. Zhang, C. Chen, J. Wang and X. Yang, Efficient, Second order accurate, and unconditionally energy stable numerical scheme for a new hydrodynamics coupled binary phase-field surfactant system. *Comput. Phys. Comm.* **251** (2020) 107122.

[57] G. Zhu, J. Kou, S. Sun, J. Yao and A. Li, Decoupled, energy stable schemes for a phase-field surfactant model. *Comput. Phys. Commun.* **233** (2018) 67–77.